# A TECHNIQUE TO MEASURE CIRRUS CLOUD EFFECTIVE PARTICLE SIZE USING A HIGH SPECTRAL RESOLUTION LIDAR

by

Ralph E. Kuehn

A thesis submitted in partial fulfillment of
the requirements for the degree of

Master of Science

(Atmospheric and Oceanic Sciences)

at the

UNIVERSITY OF WISCONSIN–MADISON

2001

Approved by: _____

Steven A. Ackerman

Professor, Atmospheric and Oceanic Sciences

Approved by: _____

Edwin W. Eloranta

Senior Scientist, Atmospheric and Oceanic Sciences

Date: _____

# ACKNOWLEDGMENTS

I would like to thank my advisor Dr. Edwin Eloranta for providing me the opportunity to work with some of the most unique and exiting lidar instruments in the world. I also appreciate all the time he has spent teaching and guiding me through this part of my education.

My thanks also go to Professors Steve Ackerman and Greg Tripoli for their thoughtful and constructive comments about this thesis to help improve the presentation of this work.

I would also like to thank all the present and past members of the University of Wisconsin Lidar Group who have helped make this work possible. A special thanks go to Partrick Ponsardin who spent hours working with me aligning the HSRL optics, Dan Forrest for helping me through many computer and electronic related problems with the HSRL and HSRL data processing, and to Bob Holz for helping me collect the data used in this thesis. I also thank Jim Hedrick for machining many new optic mounts for me and for keeping the HSRL trailer systems in good working condition. Shane Mayor also provided a lot of help with chapter 1 and a great deal of moral support during the writing process.

Finally, I would like to thank my family for their patience and support during this part of my education. Most importantly I would like to thank Nancy, my wife, for her love and support, she deserves as much credit for this work as I do.

**DISCARD THIS PAGE**

# TABLE OF CONTENTS

Page

**DISCARD THIS PAGE**

# LIST OF TABLES

**DISCARD THIS PAGE**

# LIST OF FIGURES

Appendix
Figure Page



Appendix
Figure

# ABSTRACT

High Spectral Resolution Lidar (HSRL) measurements of cirrus cloud extinction and multiple scattering are used to determine cloud effective particle size. Multiple scattering is significant in clouds because as the transmitted laser pulse travels through the cloud, half of the single scattered energy from the cloud particles is contained within the forward diffraction peak. This scattered energy propagates along with the transmitted beam and contributes to the lidar signal. The width of the diffraction peak can be determined from HSRL multiple scattering measurements, and since the diffraction peak width is proportional to the particle cross-sectional area, particle size information can be obtained. The multiple scattering contribution to the lidar signal depends on the transmitter divergence, receiver field-of-view, cloud extinction profile, effective particle size, and the scattering phase function in the backward direction. The HSRL transmitter divergence and receiver field-of-view are determined experimentally from system calibrations, and the extinction profile is provided from HSRL measurements. The effective particle size and backscatter phase function information are unknown parameters and in order to determine the effective particle size, backscatter phase function information must be provided. If the backscatter particles are molecules then the backscatter phase function information can be provided from Rayleigh scattering theory. Using the HSRL it is possible to only measure photons that have backscattered from molecules.

An approximate analytic model is used to calculate the multiple scatter contribution using the HSRL-measured extinction profile for several effective particle sizes. The model results

are then compared to the HSRL multiple scattering results to find the set of model results that best fit the HSRL data for a specific effective particle size.

Presented are the first measurements of HSRL molecular multiple scattering from February 22, 2001 in Madison, Wisconsin. Comparisons with an approximate analytical multiple scatter model indicate that the cirrus cloud observed during the period 02:17-02:41 UT had an effective radius of $70 \pm 10\mu$m, which is a reasonable value for a cirrus cloud particle size.

# Chapter 1

# Introduction

## 1.1 Motivation

Cirrus clouds are important modulators of radiation in the earth-atmosphere system because they scatter incoming solar radiation and absorb outgoing longwave radiation. Even though most cirrus clouds are optically thin, their location high in the troposphere, above most other clouds, and large global coverage ($>$ 30%, (Wylie et al., 1994)) means that their global radiative impact can be quite significant. Depending on the cloud altitude, effective particle size, and optical depth, the net radiative forcing can cool or warm the planet (Stephens and Webster, 1981). Using International Satellite Cloud Climatology Project (ISCCP) C1 cloud data and Earth Radiation Budget Experiment (ERBE) broadband energy flux data Hartmann et al. (1992) produced global estimates of cloud radiative forcing by cloud type. This analysis shows that the sign and magnitude of radiative cloud forcing varies with cloud optical depth, altitude, time of year and geographical location. However, these analyses do not provide information on how cirrus clouds respond radiatively to changes in the Earth's climate. Whether cirrus clouds warm the earth in response to global warming (positive feedback), or cool the planet (negative feedback), remains to be determined (Stephens et al., 1990; Wielicki et al., 1995; Lindzen et al., 2000).

Cirrus cloud radiative properties depend on the cloud microphysical properties, such as particle size, particle shape, and vertically integrated ice-water-content, the ice-water-path (IWP). The relationship between the microphysical and optical properties is still poorly described, because there is relatively little data of cirrus cloud microphysics properties. Little of

this data exists because measurements of cirrus cloud microphysical properties are difficult to make since the clouds are found at high altitudes and are often tenuous. More measurements of cirrus cloud microphysical and optical properties are required for a better understanding of the role of cirrus in the radiation balance of the earth-atmosphere system and to model climate change (Stephens et al., 1990).

The purpose of this thesis is to demonstrate a new method of measuring cirrus cloud effective particle size from lidar multiple scattering[1] and extinction measurements, using the University of Wisconsin High Spectral Resolution Lidar (HSRL). The effective radius is determined by measuring the width of the diffraction peak from HSRL multiple field-of-view molecular backscatter measurements. The molecular backscattering events depend only on the diffraction peak width and the extinction profile and do not depend on the shape or magnitude of the backscatter phase function of the cirrus particles. The multiple scattering contribution is significant in clouds because as the transmitted laser pulse travels through the cloud, half of the single scattered energy from cloud particles is contained within the forward diffraction peak. This scattered energy propagates along with the transmitted beam and contributes to the lidar signal (see figure 1.1). The diffraction peak width is inversely proportional to the number weighted average cross-sectional area (van de Hulst, 1957), which is directly related to the effective particle size.

The effective particle size is a representation of the cloud particle size distribution. In the most general form, the effective particle size or effective radius, $a_e$, is the number weighted average volume divided by the number weighted average cross-sectional area for an ensemble of cloud particles. For ensembles of irregularly shaped particles such as ice crystals, the exact mathematical relationship between the size distribution and the effective *radius* is somewhat obscure, since a radius is not well defined, see Wyser (1998). If the cloud particles are

[1] Multiple scattering is a term to define the physical process of a photon that scatters from more than one aerosol or molecule before returning to the lidar receiver.

spherical the effective radius can be defined as:

$$a_e = \frac{\int_0^\infty a^3 n(a) da}{\int_0^\infty a^2 n(a) da} = \frac{\langle a^3 \rangle}{\langle a^2 \rangle} \quad [1.1]$$

Where $n(a)$ is the size distribution of the cloud particles; the number of particles as a function of radius, $a$.

## 1.2 Background: Lidar Instruments and the HSRL

Light Detection and Ranging (lidar) instruments have long been used to make measurements of cloud altitude, cloud depth, aerosol[2] extinction (optical depth), and aerosol backscatter cross-section. A lidar works by sending a short pulse of light into the atmosphere, and as this pulse propagates along, some of the light is scattered back towards the receiver. For visible wavelengths of light, scattering occurs for both aerosols and molecules. The intensity of the received light is measured versus time, and since the velocity of light is known this provides a profile of the received power versus range.

A fundamental problem of traditional lidar systems is that to obtain profiles of aerosol extinction, ***a priori*** information about the relationship between backscatter and extinction must be used, where,

$$\begin{aligned} \beta_e &= \text{the extinction cross-section, per unit volume}, m^{-1}; \\ \beta' &= \beta_e \frac{\mathcal{P}_a(\pi)}{4\pi} \text{the backscatter cross-section, per unit volume}, m^{-1} sr^{-1}; \end{aligned}$$

$\mathcal{P}_a(\pi)$ is the backscatter phase function. The most notable lidar inversion technique relies on a power law relationship between backscatter and extinction (Klett, 1981). The power law is based on mathematical convenience rather than physical relationships. For example, in a given scattering volume if $\beta_e$ is fixed, the size distribution, particle shapes, and index of refraction can be changed to produce almost any value of $\beta'$. Thus, profiles of extinction generated using

[2] In this paper aerosols include both cloud droplets/crystals and macroscopic airborne particles (dust, pollen, soot, etc.)

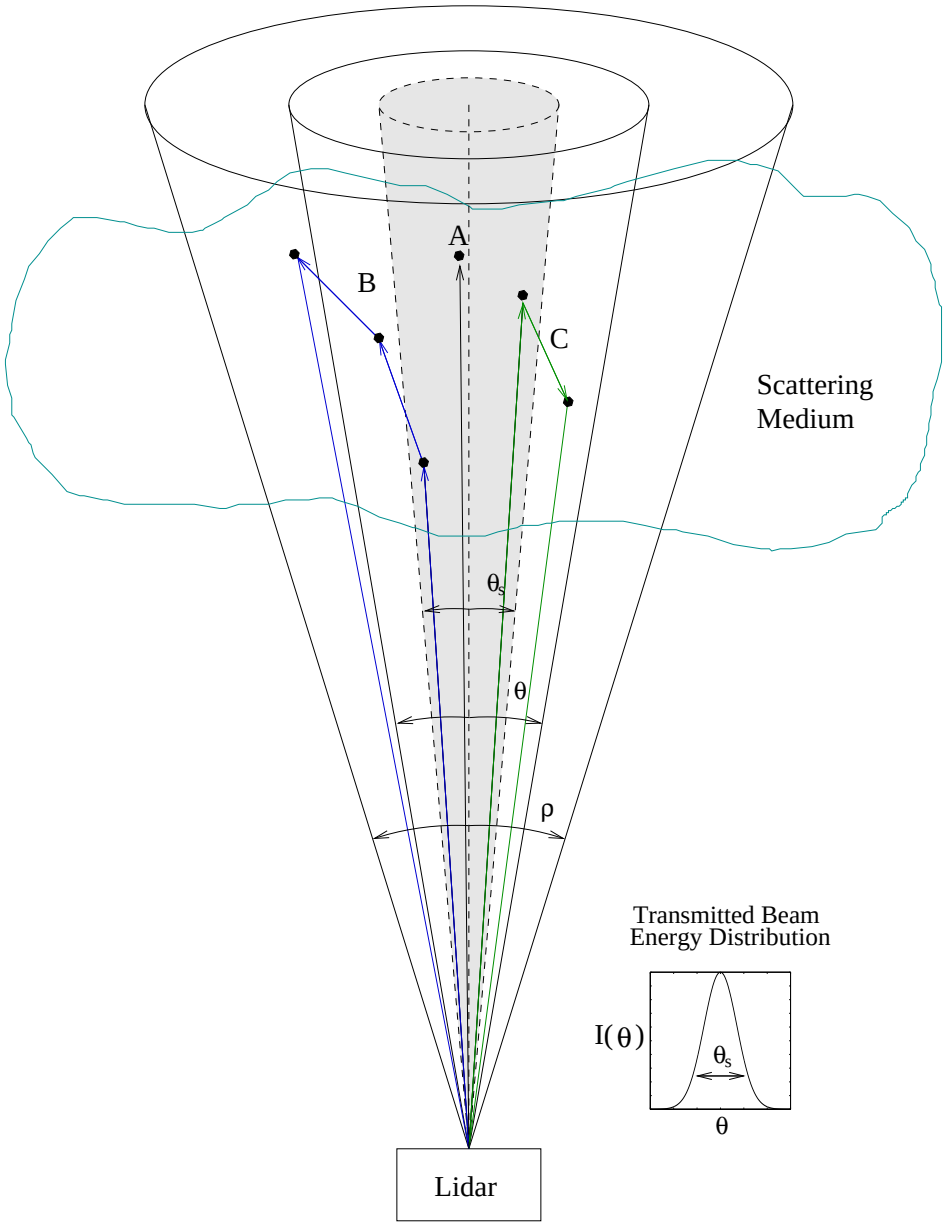


Figure 1.1 Lidar scattering geometry. The grey shaded area represents the angular distribution of transmitted energy of the laser transmitter, $\theta_s$ is the $e^{-1}$ point of the distribution, I is the radiance, $W \cdot m^{-2} sr^{-1}$. The angles $\theta$ and $\rho$ represent the narrow, and wide field-of-view of the receiver. The photon path $A$ shows a single scatter event. $B$ and $C$ show examples of possible photon trajectories that scatter from more than one particle (multiple scattering). $B$ shows a trajectory where the photon backscattered on the *last* event before returning to the receiver. $C$ shows a photon path where the photon backscatters *before* higher order scattering events.

the Klett method may have large errors (Mitev et al., 1992). The HSRL was developed to overcome this fundamental limitation by separating the received signals into their molecular and aerosol scattering components, (Shipley et al., 1983; Grund, 1987; Piironen, 1994). Using Rayleigh scattering theory and an atmospheric temperature and density profile, the measured molecular signal provides a known target at each altitude from which the aerosol backscatter cross-section can be determined. The aerosol extinction profile can also be determined by comparing the measured molecular signal to the molecular signal calculated in the absence of aerosol extinction. Error bars can be calculated for each data product without relying on assumed relationships between extinction and backscatter, because these measurements depend only on statistical (photon counting) errors, system alignment errors, and calibration errors.

Also, lidar systems that can measure molecular Raman scattering can provide calibrated profiles of aerosol extinction and backscatter.

## 1.3 Lidar Multiple Scattering

When making atmospheric measurements with a lidar system, the multiple scattering contribution is usually treated as an error term when deriving the extinction profile. The capability of the HSRL to measure the multiple scatter contribution for several receiver fields-of-view allows this "error" term to be utilized as a powerful source of information about the cloud microphyics. Eloranta (1967) conducted some of the earliest multiple scattering lidar research, and provided both the mathematical framework for modeling the double scattered lidar return and made model comparisons with lidar measurements of fogs and hazes. Eloranta (1967) also showed that the size distribution, $n(a)$, of fogs and hazes could be determined using this method. Also, at that time it was still not generally accepted nor understood that multiple scattering contributed significantly to the single scattered lidar return thus affecting measurements of extinction and backscatter. Work by Liou and Schotland (1971) seemed to indicate that the multiple scattering contribution would in fact be small compared to the single scattered lidar return, even for large receiver fields-of-view (FOV). This result was contradicted and

found to be incorrect by the work of Eloranta (1972), who presented an exact analytical solution for double scattered photons and showed that the multiple scatter contribution would be roughly ten times greater than that presented by Liou and Schotland (1971). Eloranta (1972) had also suggested that it may be possible to determine the width of the forward diffraction peak with lidar measurements. Since then several investigators have developed models that can describe the multiple scattering contribution as a function of receiver FOV, transmitter divergence, cloud optical depth, effective particle size and scattering phase function in the backscatter direction. (Eloranta, 1998; Bissonnette, 1996).

Several investigators have also demonstrated the use of lidar multiple scattering measurements to determine the effective radius, $a_e$, and the particle size distribution, $n(a)$, of clouds. Allen and Platt (1977) presented a description and measurements from single channel lidar system. They showed that multiple scattering from water and cirrus clouds could be measured, and that it varied with receiver FOV. Later, Bissonnette and Hutt (1995); Roy et al. (1997) demonstrated that lidar multiple scattering measurements could provide $a_e$, and $n(a)$ for water clouds, and made comparisons with aircraft *in situ* measurements. These measurements, while successful, have been limited to clouds at low altitudes ($< 2km$), because of instrument limitations. Benayahu et al. (1995) also reported a technique to measure the cloud droplet size distribution, $n(a)$, in water clouds. This technique required near horizontal pointing direction for the lidar so as to probe the cloud from the side, so $n(a)$ would not vary with range (i.e. altitude). They only considered second order scattering, and were limited to small optical depths. Yet another technique is described by Roy et al. (1999) to measure $n(a)$, at cloud base from lidar measurements of depolarization as a function of the receiver FOV. This method however assumes the cloud is optically thin (optical depth $< 1$), since only second order scattering is considered, and that the scattering particles are spherical.

The particle size measurement techniques presented above require information about the backscatter phase function, $\mathcal{P}(\pi)$, of the backscattering particles in order to determine $n(a)$, or $a_e$. This is a necessary requirement, since the photons that are most likely to contribute to the lidar signal undergo only one large angle scattering event, (i.e. the scattering angle,

$\theta_s$, $\approx \pi$). For single scattering the photons that contribute scatter precisely at an angle of $\pi$, so the single scattered return depends on $\mathcal{P}(\pi)$. The multiple scattered lidar signal must also depend on $\mathcal{P}(\theta_s \approx \pi)$, and for most multiple order scatter events the backscattering angle will be less than $\pi$ in order to return the photon to the receiver. The result is that the multiple scattered signal depends on both $\mathcal{P}(\pi)$, and $\langle \mathcal{P}(\pi) \rangle_n$. Where $\langle \mathcal{P}(\pi) \rangle$ is the average backscatter phase function of the backscattering particles, encountered by the multiple scattered photons of scattering order, $n$. Since the multiple scatter contribution depends on both the width of the forward diffraction peak and $\langle \mathcal{P}(\pi) \rangle$, $\langle \mathcal{P}(\pi) \rangle$ must be assumed or measured so the width of the forward diffraction peak can be determined. If the backscattering particles are spherical aerosols and a size distribution is specified, Mie theory can provide backscatter phase function information. For irregularly shaped aerosols such as ice crystals, the particle shapes and size distribution information is necessary to provide the backscatter phase function. Even with this information, the phase function could only be modeled[3], or perhaps estimated from laboratory measurements. However, if the backscattering particles are molecules, the scattering phase function is known to be nearly isotropic. Both $\mathcal{P}(\pi)$ and $\langle \mathcal{P}(\pi) \rangle$ are provided by Rayleigh scattering theory.

## 1.4 The Technique

The technique presented in this thesis utilizes the ability of the HSRL to simultaneously measure multiple scattered photons backscattered from atmospheric molecules and cloud extinction. An approximate multiple scatter model (see section 3.3) is used to calculate the multiply scattered lidar return as a function of the receiver FOV and particle size, given the parameters of the cloud extinction profile, receiver FOV, and transmitter divergence. Then, $a_e$ is used as a variable to optimize the fit between HSRL observations and the model data. When the model results are in agreement with the observations, the value of $a_e$ used for the model calculations is assumed to represent $a_e$ of the cloud.

[3]This is an enormous field of study, the details of which are beyond the scope of this thesis. Much information about this topic can be found in Mishchenko et al. (2000)

## 1.5 Overview

This section provides a brief overview of the remaining chapters of this thesis. In chapter 2, lidar theory and HSRL principles will be discussed. Chapter 3 will describe three different multiple scattering models, the last of which is a Monte Carlo scheme. The last section shows a numerical comparison of the models. Chapter 4 will describe the method for HSRL multiple scattering measurements and how to present the data so that it can be easily compared with the multiple scattering model results. Chapter 5 shows the first HSRL measurements of molecular multiple scattering from 22 February 2001 in Madison, Wisconsin, and the profiles of cloud extinction necessary to run the multiple scatter model. Chapter 6 shows the model results from 22 February 2001, and Chapter 7 presents a comparison of the model results and HSRL measurements.

# Chapter 2

# Theory

## 2.1 Introduction

The purpose of this chapter is to provide the background information necessary to understand how profiles of extinction cross-section , optical depth, backscatter cross-section, and depolarization are derived from HSRL measurements. Starting with a general form of the lidar equation, the molecular and aerosol components can be separated allowing these parameters to be derived. Two methods are included to derive the optical depth. The first, termed the simple optical depth, depends only on the measured molecular signal, and is sensitive to multiple scattering contributions to the lidar signal. The second method uses a vertically averaged value of the backscatter phase function to derive the extinction profile, and if the cloud is transparent to the lidar then the uncertainty in the derived extinction profile, from multiple scatter contributions, will be significantly reduced.

## 2.2 Lidar Equation

This section defines the lidar equation, shown in terms of the number of received photons, rather than power received. A derivation of this equation can be found in Measures (1988).

$$N(r,fov) = F(r,fov)N_o(fov)\frac{cA}{2r^2}\left(\frac{3}{8\pi}\beta_m(r)+\beta_a(r)\frac{\mathcal{P}_a(\pi,r)}{4\pi}\right)e^{-2\tau(r)}+M(r,fov)+b(fov) \quad [2.1]$$

where,

$N(r,fov)$ = number of photons incident on the receiver from range r, inside FOV, $fov$;

$F(r, fov)$ = a geometrical factor, which depends on the receiver optics and the transmitter beam divergence;

$N_o(fov)$ = number of transmitted photons within the FOV, $fov$;

$c$ = speed of light, $ms^{-1}$;

$A$ = area of receiver, $m^2$;

$\beta_a(r), \beta_m(r)$ = aerosol and molecular scattering cross sections per unit volume from range r, respectively, $m^{-1}$

$\frac{3}{8\pi}$ = molecular backscatter phase function, $sr^{-1}$;

$\frac{\mathcal{P}_a(\pi, r)}{4\pi}$ = aerosol backscatter phase function from range r, $sr^{-1}$;

$\tau(r)$ = optical depth of the layer between ranges $r_1$, and $r_2$, is given by $\int_{r_1}^{r_2} \beta_e(r')dr'$,

$\beta_e(r)$ = total extinction cross section per unit volume at range r, $m^{-1}$;

$M(r, fov)$ = multiple scattering contribution (See section 3);

$b(fov)$ = background signal;

The dependence of the terms $N(r, fov)$, $M(r, fov)$, $b(fov)$ and $F(r, fov)$ on FOV is explicitly indicated in this work, since the HSRL operates with several receiver FOVs, not just one fixed receiver FOV. The term $F(r, fov)$ accounts for the fact that at close ranges the telescope is out of focus. This is a dimensionless quantity and is less than unity within 4 km of the HSRL receiver.

The HSRL is able to separate the molecular and aerosol signals by transmitting a spectrally narrow laser pulse, which is tuned to an absorption line of iodine gas. Thermal motion of atmospheric molecules Doppler broaden the spectrum of the backscattered photons. The aerosols which are much heavier and moving more slowly do not shift the backscattered spectrum significantly. Aerosol scattering is removed from one HSRL channel by removing the center of the returned spectrum with an iodine gas absorption filter. (See figure 2.1).

## 2.3 HSRL Principles

The signals measured by the HSRL are $S_M$ and $S_{A+M}$. $S_M$ is called the molecular channel, since most of the photons measured by this channel have backscattered from molecules. There is some leakage into this channel from photons that have backscattered from aerosols, because not all the aerosol photons are absorbed by the iodine filter. $S_{A+M}$ is the combined channel, measuring all molecular and aerosol photons. These signals can be inverted to provide the individual aerosol and molecular signals as a function of range. The inversion requires system coefficients derived from a spectral scan across the iodine absorption line while recording the signals from both channels (Piironen, 1994). If the background light is subtracted from the lidar signals and multiple scattering is ignored, the lidar equation above can be written:
For aerosols,

$$N_a(r, fov) = F(r, fov)\frac{N_o(fov)cA}{2r^2}\beta_a(r)\frac{\mathcal{P}_a(\pi, r)}{4\pi}e^{-2\tau(r)} \quad [2.2]$$

For molecules,

$$N_m(r, fov) = F(r, fov)\frac{N_o(fov)cA}{2r^2}\beta_m(r)\frac{3}{8\pi}e^{-2\tau(r)} \quad [2.3]$$

From these two equations the following parameters can be derived.
The scattering ratio:

$$SR(r) = \frac{N_a(r)}{N_m(r)} \quad [2.4]$$

$SR(r)$ does not depend on FOV, since the terms that depend on FOV in both equations of $N_a(r, fov)$ and $N_m(r, fov)$, cancel.
The aerosol backscatter cross-section:

$$\beta'_a(r) = \beta_a(r)\frac{\mathcal{P}_a(\pi, r)}{4\pi} = SR(r)\beta_m(r)\frac{3}{8\pi} \quad [2.5]$$

The simple optical depth:

$$\tau_s(r) \quad = \quad -\frac{1}{2}\log\left(\frac{N_m(r, fov)}{N_T(r)}\right) \quad [2.6]$$

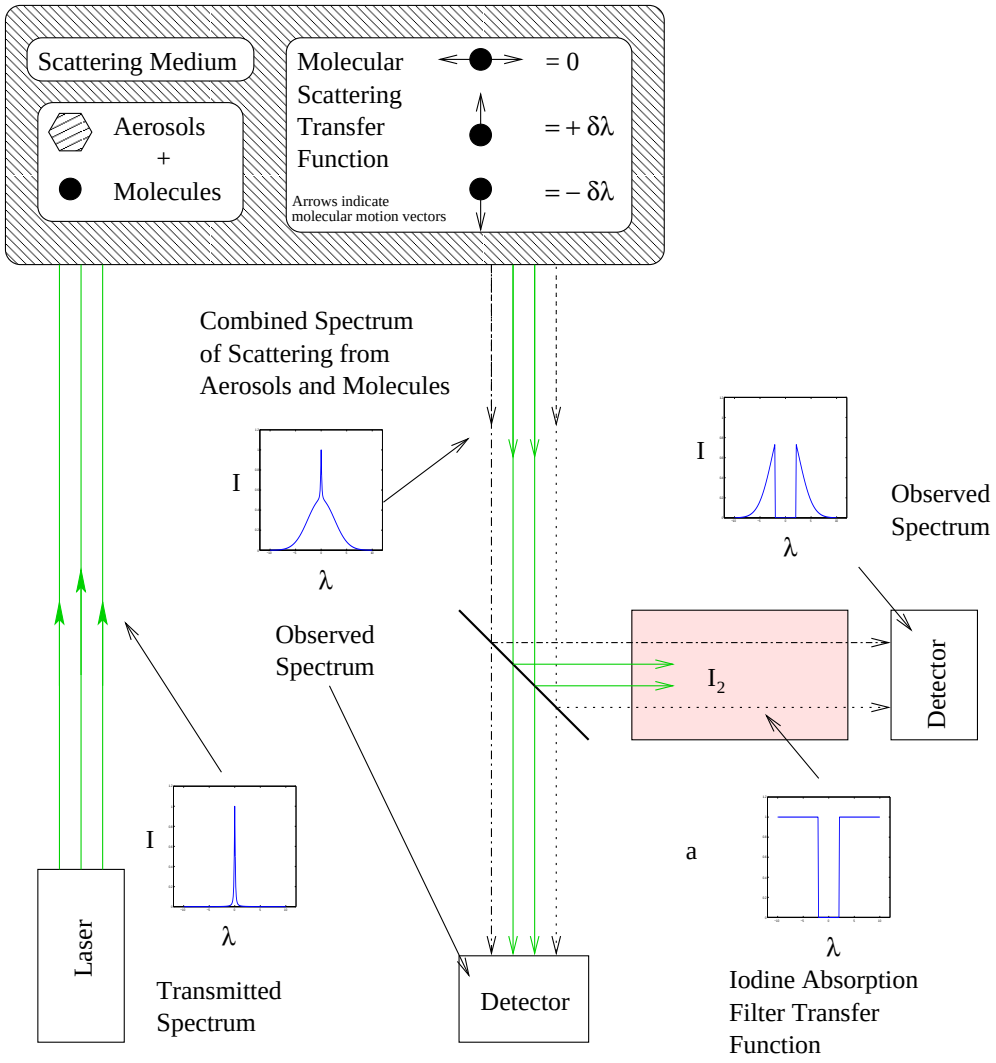


Figure 2.1 Spectral diagram of the HSRL transmitter and receiver: The laser transmitter produces a spectrally narrow pulse of light. This pulse back-scatters from molecules and aerosols; the molecules which are moving relatively fast compared to the aerosols produce a Doppler shift in wavelength of the scattered photons. The combined signal received by the HSRL is split between two detectors. The first measures the entire atmospheric signal. The second detector with the iodine absorption filter, will receive photons whose wavelength has been Doppler shifted so that they are not absorbed by the iodine gas. This detector only receives photons backscattered from molecules.

$$N_T(r) \quad \propto \quad F(r, fov)\frac{N_o(fov)cA}{2r^2}\beta_m(r)\frac{3}{8\pi}$$

where the term $N_T(r)$ is the derived molecular signal is the absence of aerosol extinction . $N_T(r)$ is calculated using pressure and temperature profiles provided by radio sonde measurements, and molecular scattering theory. $N_T(r)$ is then scaled to the molecular profile $N_m(r, fov)$ at a range, $r_o$, which is above the lidar overlap region (i.e. $F(r, fov) = 1$, above 4 km). $\tau_s$ is given the subscript *s* to designate it as the simple optical depth. Note that the simple optical depth is the optical depth from the range, $r_o$, not from the lidar.

The aerosol extinction profile may be calculated from $\tau_s(r)$ by,

$$\langle\beta_a(r)\rangle = \frac{\tau_s(r_2) - \tau_s(r_1)}{r_2 - r_1} \qquad [2.7]$$

Where $\langle\beta_a(r)\rangle$ is the average value of $\beta_a$ between range bins $r_1$ and $r_2$.

$\beta_a(r)$ may also be determined in another way and will minimize errors from multiple scatter contributions as long as the total cloud optical depth does not exceed 3.0, the maximum optical depth measurable with the HSRL. The following equation,

$$\int_{r_1}^{r_2} \frac{\beta'_a(r)}{\left\langle\frac{\mathcal{P}_a(\pi)}{4\pi}\right\rangle}dr = \tau_s(r_2) - \tau_s(r_1) \qquad [2.8]$$

will be satisfied when the correct value of the bulk backscatter phase function of the cloud particles, $\langle\mathcal{P}_a(\pi)\rangle/4\pi$ is used, $r_1$ is the altitude of the cloud base, and $r_2$ is an altitude several kilometers above the cloud top where multiple scatter contributions to the signal $N_m(r, fov)$ are small. Figure 2.2 shows a comparison of the integral in equation 2.8 using $\langle\mathcal{P}_a(\pi)\rangle/4\pi = 0.027$ and a profile of $\tau_s(r)$ derived from HSRL measurements. Then the profile of $\beta_a(r)$ is calculated from,

$$\beta_a(r) = \frac{\beta'_a(r)}{\left\langle\frac{\mathcal{P}_a(\pi)}{4\pi}\right\rangle} \qquad [2.9]$$

By calculating $\beta_a(r)$ in this manner the error from multiple scattering contributions to the the single scattered lidar signal can be minimized. The multiple scatter contribution to the signals $N_a(r, fov)$ and $N_m(r, fov)$ are proportional to the individual single scatter signals.

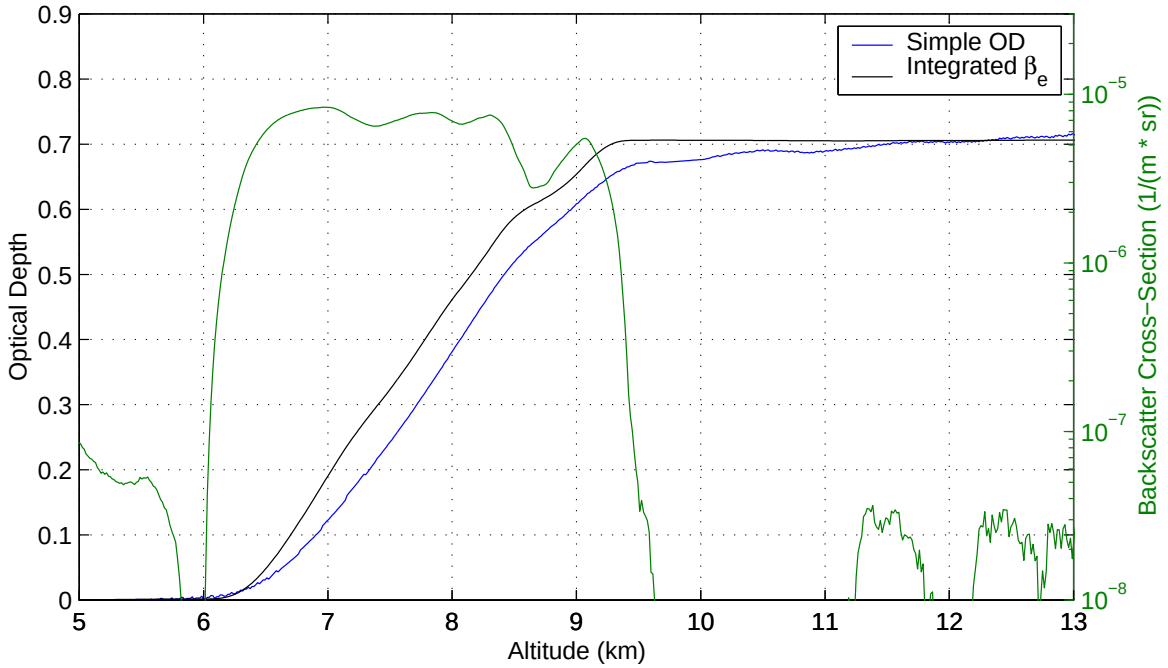


Figure 2.2 An example of the simple optical depth, $\tau_s(r)$, and the integrated extinction profile, $\tau(r)$, derived from HSRL measurements on 2/22/01. Also, plotted along with the profile of $\beta'_a(r)$. The effect of multiple scattering on the profile of $\tau_s$ is seen as a systematic decrease in the optical depth in and above the cloud.

Therefore the value of $SR(r)$ is relatively insensitive to multiple scattering effects. Used alone, the multiple scatter contribution to the molecular signal $N_m(r)$ is significant enough that in calculating the optical depth from equation 2.6 (i.e the simple optical depth) results in a systematic decrease in the optical depth in and above the cloud, until 2-3km above the cloud top where multiple scatter contributions are small. For example, figure 2.2 shows the simple optical depth $\tau_s(r)$, is biased from multiple scattering contributions while the contribution to the integrated extinction profile is small.

Finally, in the aforementioned definitions, the aerosol signal $N_a(r, fov)$ is defined as a single parameter, the HSRL however, also measures the change in the polarization state of the received photons. The receiver separately measures the number of parallel $(\|)$ and perpendicular $(\perp)$ polarized photons with respect to the transmitted linear polarization. Given the

measurements $N_{a\parallel}(r, fov)$ and $N_{a\perp}(r, fov)$ the quantity $\delta$, the depolarization, is defined as:

$$\delta = \frac{N_{a\perp}(r, fov)}{N_{a\parallel}(r, fov)} \quad [2.10]$$

This quantity is useful for unambiguously classifying the phase of the cloud particles. Since water droplets are spherical, photons that backscatter from water droplets have the same polarization. Depolarization measurements of water clouds typically range from 0.01 to 0.05. Since ice crystals are irregularly shaped the polarization state of the scattered photon is rotated with respect to the incident polarization. Depolarization values from ice range from 0.25-0.5. These depolarization values represent measurements from the UW HSRL which has been designed to minimize the multiple scatter contribution in the channels responsible for depolarization measurements. Therefore, these depolarization values are not directly comparable to measurements with lidar systems that have different receiver FOVs. The depolarization ratio will increase as multiple scattering increases, so measurements using larger receiver FOVs may not be able to unambiguously classify cloud phase.

# Chapter 3

# Multiple Scattering

## 3.1 Introduction

The measured lidar signal consists of both single and multiple scattered photons. The multiple scattering contribution is significant when there are clouds in or below the scattering volume, relative to the lidar. This is because as the transmitted laser pulse travels through the cloud layer, half of the energy scattered by the cloud particles is contained within the forward diffraction peak. This energy propagates along with the transmitted beam and contributes to the lidar signal. At this time an exact analytic solution that describes the amount of multiple scattering does not exist. However, there are several approximate models that can accurately describe lidar multiple scattering.

The rest of this chapter is dedicated to describing two models based on analytical approximations for multiple scattering and one Monte Carlo model. The final section shows the results of a numerical comparison between all three models.

## 3.2 Infinite FOV Model

The approximate analytical solution to lidar multiple scattering formulated by Eloranta and Shipley (1982) is dubbed in one of its forms as the infinite FOV model. When the FOV is assumed to be large compared to the diffraction peak width of the particles the multiple scatter contribution can be determined very easily.

First the *finite* FOV solution is given as,

$$\frac{P_n(r)}{P_1(r)} = 2^{n-1}\langle\alpha\rangle^{n-1}\frac{\langle\mathcal{P}(\pi)\rangle}{\mathcal{P}(\pi)}A_n\frac{\tau(r)^{n-1}}{(n-1)!} \quad [3.1]$$

where $P_n$ is the lidar signal from $n^{th}$ order scattering. $\langle\alpha\rangle$ is the fraction of the total energy contained in the forward diffraction peak spatially averaged in height through the cloud. $\langle\mathcal{P}(\pi)\rangle$ is the average value of the phase function near $180^o$ encountered during a single backscattering event (Eloranta and Shipley, 1982). For both irregularly shaped particles and spheres the ratio $\langle\mathcal{P}(\pi)\rangle/\mathcal{P}(\pi)$ is generally less than 1. For isotropic backscatterers (.i.e. molecules) $\langle\mathcal{P}(\pi)\rangle/\mathcal{P}(\pi) = 1$. $A_n$ is a dimensionless coefficient that controls the amount of multiple scattering as a function of lidar geometry and the cloud particle diffraction peak width. $A_n$ is a function of the parameter,

$$T^2 = \frac{\theta^2}{\langle\theta_s^2\rangle}(\frac{r}{r-r_c})^2 \quad [3.2]$$

and the scattering order $n$. Where $\theta$ is the receiver FOV, $\langle\theta_s^2\rangle$ is the mean square angle for forward scattering, $r_c$ is the cloud base altitude, and $(r - r_c)$ is the penetration depth into the cloud. The relationship between $T^2$ and $An$ is such that as $T^2$ increases $An$ increases. When $T^2 \gg 1$, $An \approx 1$. Equations 3.1 and 3.2 show that for a given value of the transmitter divergence, multiple scattering increases with the penetration depth, larger values of $\tau$, and increasing receiver FOV. Also, to minimize the effects of multiple scattering on the calculation of $\beta_a'(r)$ and $\tau(r)$ the transmitter divergence and receiver FOV should be as small as possible.

It should be noted that even when the receiver FOV is small, at cloud base $r \approx r_c$ and $T^2 \rightarrow \infty$, and $An = 1$. This has a significant physical meaning, at cloud base all of the multiple scatter return is contained within the receiver FOV. As discussed in section 2.3 this contributes to the single scattered lidar return in the narrowest receiver FOV and can bias measurements of the simple optical depth. For optically thick clouds or any case where $T^2$ is large, the multiple scattering contribution can be quite significant.

For the case where the receiver FOV $\gg \langle\theta_s^2\rangle$, $A_n \rightarrow 1$, and if half of the scattered energy is contained within the forward diffraction peak $\langle\alpha\rangle = 1/2$, then equation 3.1 reduces to the

infinite FOV equation:

$$\frac{P_n(r)}{P_1(r)} = \frac{\langle \mathcal{P}(\pi) \rangle}{\mathcal{P}(\pi)} \frac{\tau(r)^{n-1}}{(n-1)!} \qquad [3.3]$$

Equation 3.3 depends on both the optical depth and the backscatter phase function ratio. If the backscattering particles have an isotropic backscatter phase function, then this ratio is one and the multiple scatter contribution depends only on the optical depth.

## 3.3 Gaussian Approximate Solution

The multiple scattering model describe here was developed by Eloranta (1998) and is in fact a derivative of the infinite FOV model. This model is referred to as the Gaussian model. Like the infinite FOV model the primary assumption is that each photon experiences *only one large angle scattering event*. This means that photons are assumed to be scattered within the forward diffraction peak and in the backscatter direction. No other photons are considered. Given this assumption the ratio $\langle \mathcal{P}(\pi) \rangle / \mathcal{P}(\pi)$ is again used as a parameter. For isotopic backscatters, like molecules, this ratio equals one. The second assumption is that a Gaussian function represents the forward scattering diffraction peak. The form is:

$$\frac{\mathcal{P}(\theta)}{4\pi} = \frac{\mathcal{P}(0)_{true}}{4\pi} exp\left(-\frac{\theta^2}{\theta_s^2}\right) \qquad [3.4]$$

Where $\mathcal{P}(0)_{true}/4\pi$ is the value of the phase function at zero degrees provided by Mie theory or calculated as a function of the effective particle size. The value of $\theta_s$ is determined explicitly from the value $\mathcal{P}(0)$ if we assume that equation 3.4 is integrated over the sphere and is equal $\frac{1}{2}$, or rather that the diffraction peak contains half of the scattered energy. So,

$$\int_{4\pi} \frac{\mathcal{P}(\theta)}{4\pi} d\Omega = 1/2$$

yields,

$$\langle \theta_s^2 \rangle = \frac{2}{\mathcal{P}(0)} \qquad [3.5]$$

To generalize this for any arbitrary distribution of particle sizes $n(a)$, the scattering cross section $\beta_s$ can be defined as,

$$\beta_s[\lambda_o, n(a)] = \pi \int_{a_1}^{a_2} a^2 n(a) Q_{sc}(\lambda_o, a) da \qquad [3.6]$$

where $Q_{sc}$ is the scattering efficiency factor. Then the average value of the phase function at zero degrees may be calculated in following way after Deirmendjian (1969),

$$\mathcal{P}(0) = \frac{4\pi}{k^2 \beta_s} \int_{a_1}^{a_2} n(a) I(0, a) da \qquad [3.7]$$

If we assume that the particles are large so that $Q_{sc}(\lambda_o) = 2$ and $I(0, a) = k^4 a^4/8$, where $k = 2\pi/\lambda$, then equation 3.7 becomes:

$$\mathcal{P}(0) = \frac{\frac{\pi k^2}{2} \int_{a_1}^{a_2} \frac{a^4}{8} n(a) da}{2\pi \int_{a_1}^{a_2} a^2 n(a) da} = \frac{\langle a^4 \rangle}{\langle a^2 \rangle} \frac{2\pi^2}{\lambda^2}$$

$$a_e \approx \frac{\lambda}{\pi} \sqrt{\frac{\mathcal{P}(0)}{2}} \qquad [3.8]$$

Where, $a_e = \frac{\langle a^3 \rangle}{\langle a^2 \rangle}$ and the following assumption has been made: $a_e \approx \sqrt{\frac{\langle a^4 \rangle}{\langle a^2 \rangle}}$. This approximation is surprisingly robust and is not limited to the previous assumption that the particles are spherical. Since in general the value of the scattered intensity $I(0)$ in the forward direction depends primarily on the cross-sectional particle area. For the remainder of this thesis the effective particle size will be represented by $a_e$.

Assuming that the diffraction peak contains half of the forward scattered energy, has a Gaussian shape, and $\mathcal{P}(0) = 2/\langle \theta_s \rangle$, it is possible to derive an equation describing the ratio of returned power of scattering order $n$, divided by the single scattered returned power, $P_n(r)/P_1(r)$. This ratio must be evaluated numerically and can be calculated given the following input parameters, $\beta_e(r)$, $a_e$, $\beta_m(r)$, the receiver FOV, and $\theta_t$ the laser transmitter divergence (full-angle). The numerical model used for the multiple scatter calculations has been fully implemented by Eloranta, and the results computed for this paper were calculated using this software.

## 3.4 Monte Carlo

This section describes the Monte Carlo simulation of lidar multiple scattering. The name Monte Carlo comes from the city bearing that name and generally defines a statistical method of evaluating mathematical or physical systems. This Monte Carlo simulation was developed to investigate multiple scattering for lidar systems that are difficult or impossible to solve by other approximate analytical models. The main purpose of this Monte Carlo was to validate the Gaussian model, and the Gaussian model software. Part one gives a general overview of this Monte Carlo, and part two describes the model in more detail.

### 3.4.1 Overview

In this application of the Monte Carlo method one photon is propagated at a time into the atmosphere. The probability of when the photon scatters depends on the prescribed extinction profile. The scattering angle of each event is determined by Mie or Rayleigh scattering theory, depending whether the scattering particle is an aerosol or molecule. Instead of propagating each photon indefinitely until it returns to the receiver, at each scattering event the photon is assumed to have returned to the receiver and is weighted according to the probability of that event occurring. The photon is then scattered randomly and propagated to the next scatter event, where it is again assumed to have returned to the receiver. At each scattering event the photon properties are accumulated according to the FOV, range, scattering order, and polarization. This methodology was chosen to minimize the number of accumulated photons necessary for a statistically significant multiple scattered signal, compared to a traditional random walk scheme.

Even though this model calculates the partial return at each scattering event, photons that have backscattered before a higher order scattering event and remain within the receiver FOV, are rare (type C, see figure 1.1). The example in figure 1.1 shows just one type C trajectory, a forward-back-forward trajectory would also be considered type C for third order scattering. In the real atmosphere these types of photon trajectories are just as likely to occur as those

trajectories where on the last event the photon is backscattered (type B), so type C's are just as significant. Just considering double scatter events it is evident that type B and C photons will contribute equally to the multiple scattered signal. The joint probability of forward-back scattering and back-forward scattering are equal so they must contribute equally to the second order scattered signal. In the Monte Carlo, the back-forward (type C) must backscatter purely by chance, and the probability of backscattering towards the receiver is tiny. The model must propagate many billions of photons until a statistically significant sample of the type C photons are accumulated.

### 3.4.2 Model Detail

The simulation uses a Stokes vector to represent the photon polarization state and each photon is transmitted with a linear polarization so the initial Stokes vector is defined as:

$$\begin{bmatrix} I \\ Q \\ U \\ V \end{bmatrix} = \begin{bmatrix} 1 \\ 1 \\ 0 \\ 0 \end{bmatrix} \qquad [3.9]$$

Scattering events are computed by multiplying the Stokes vector by the Mueller matrix of scattering angle $\phi_s$. Since the Stokes vector is rotated into a new plane at each scattering event, each photon is also described by set of basis vectors, these two vectors represent orientation of the photons coordinate system relative to the receiver.

The simulation begins by loading the extinction profile of the cloud, the temperature and density profile, and the Mueller matrix elements for each scattering angle for the cloud aerosol. If the cloud type being modeled is water or consists of a distribution of particle sizes, phase function values are calculated using Mie theory. Alternatively, the phase function values may be generated using a Gaussian approximation along with a constant value for the phase function in the backscatter direction. Also, when the Gaussian approximation is used, the Mueller matrix components, $M_2$, $M_3$, and $M_4$, are set to zero for all angles. For molecules, the Mueller

matrix is calculated using:

$$\begin{aligned} M_1(\phi) &= \frac{1}{2}(1 + cos(\phi)^2); \\ M_2(\phi) &= \frac{1}{2}(cos(\phi)^2 - 1) \\ M_3(\phi) &= cos(\phi) \\ M_4(\phi) &= 0.0 \end{aligned} \quad [3.10]$$

The probability distributions for choosing the scattering angle and the scattering distance are also created. These are lookup tables generated so that only random numbers are necessary at each scattering event to determine the scattering angle and distance traveled. The main program loop has the following structure.

1. Pick initial direction based on transmitted Gaussian energy distribution.
2. Move photon to cloud base.
3. Pick random number to determine distance to scattering event. (From probability distribution generated from extinction profile).
4. Move photon to scattering particle.
5. Determine if photon is within the receiver FOV.
6. Determine if particle is an aerosol or molecule. (From scattering cross-sections.)
7. Now assume photon scatters back to receiver.
   (a) Calculate scattering angle $\phi_s$ back to receiver.
   (b) Rotate photon Stokes vector into scattering plane, angle $\psi$. (For scattering orders $> 2$. The plane is defined by last and current scattering particle and the receiver.)
   (c) Multiply photon Stokes vector by Mueller matrix $M(\phi_s)$.

(d) Calculate probability of photon traveling along this path back to receiver without being extinguished. This becomes the photon weight.

$$w = \frac{cos(\Phi)}{r'^2} e^{-\tau(z)} \quad [3.11]$$

Where $\Phi$ is the angular location of the photon with respect to the z-axis. $r'$ is the distance from the receiver to the photon, and $\tau(z)$ is the optical depth from the altitude $z$ to the receiver.

(e) Move photon to receiver.

(f) Rotate photon Stokes vector into original coordinate system of receiver.

(g) Record photon properties binned according to total distance traveled, scattering order, and FOV:

$$\begin{aligned} P(l,n,fov) &\propto w \cdot I \\ P_{\perp}(l,n,fov) &\propto w \cdot \frac{(I-Q)}{2} \\ P_{\parallel}(l,n,fov) &\propto w \cdot \frac{(I+Q)}{2} \end{aligned} \quad [3.12]$$

$l$ and $n$ are the path length and scattering order, respectively. The last two expressions account for the linear polarization state of the received photon in terms of the $\perp$ and $\parallel$ components with respect to the transmitted polarization.

Let photon continue along its original path.

8. Determine scattering angle, $\phi_s$, from phase function probability distribution and load appropriate Mueller matrix, $M(\phi_s)$.

9. Rotate photon Stokes vector into scattering plane, angle $\psi$. (Picked from uniform probability distribution.)

10. Multiply Stokes vector by Mueller matrix, $M(\phi_s)$.

11. Normalize Stokes vector by component I.

12. Return to step 3.

The rotation and multiplication steps are performed using the following matrix multiplication (steps 7b,7c and 9, 10)

$$\begin{bmatrix} I \\ Q \\ U \\ V \end{bmatrix} = \begin{bmatrix} M_0 & M_1 & 0 & 0 \\ M_1 & M_0 & 0 & 0 \\ 0 & 0 & M_2 & M_3 \\ 0 & 0 & -M_3 & M_2 \end{bmatrix} \begin{bmatrix} 0 & 0 & 0 & 0 \\ 0 & cos(2\psi) & -sin(2\psi) & 0 \\ 0 & sin(2\psi) & cos(2\psi) & 0 \\ 0 & 0 & 0 & 0 \end{bmatrix} \begin{bmatrix} I_0 \\ Q_0 \\ U_0 \\ V_0 \end{bmatrix} \quad [3.13]$$

Step 11, the Stokes vector normalization, is done to preserve the continuity that only one photon is propagated at a time and the photon polarization state.

## 3.5 Model Comparison

This section shows a comparison of the Monte Carlo and multiple scattering models. This was necessary because both the Monte Carlo and the Multiple Scatter model code had not been rigorously tested for coding errors. A hypothetical cloud was created to perform this comparison. The cloud optical and simulated lidar parameters used were:

Table 3.1 Cloud Optical Properties

| | |
|---|---|
| Base | 600 m |
| Top | 900 m |
| $a_e(r)$ | uniform, 25 $\mu$ m |
| $\beta_a(r)$ | uniform, $3.33x10^{-3}(m^{-1})$ |
| Total $\tau$ | 1.0 |

Table 3.2 Transmitter, Receiver Specifications

| | |
|---|---|
| Transmitter Div. (Gaussian) | 110 $\mu$ rad |
| Receiver FOVs (wide 1) | 10.3 mrad |
| (wide 2) | 963 $\mu$ rad |
| (wide 3) | 296 $\mu$ rad |
| (narrow) | 110 $\mu$ rad |

The cloud properties were chosen to minimize the time required to accumulate a statistically significant signal from multiple scattered photons in the Monte Carlo model. It was necessary to accumulate $4.8 \cdot 10^{10}$ photons to generate good statistics.

The Monte Carlo model run consisted of 8 separate model runs of $6.0 \cdot 10^9$ photons each. The total computer time required was approximately 65 hours, see appendix A for computer details. Figure 3.2 shows a comparison of the Monte Carlo, Gaussian, and infinite FOV models. The Monte Carlo results show the mean value of $P_n/P_1$ for 2nd, 3rd, and 4th order scattering. The error bars estimate $\pm\sigma$, the standard deviation in the mean, for all the model runs.

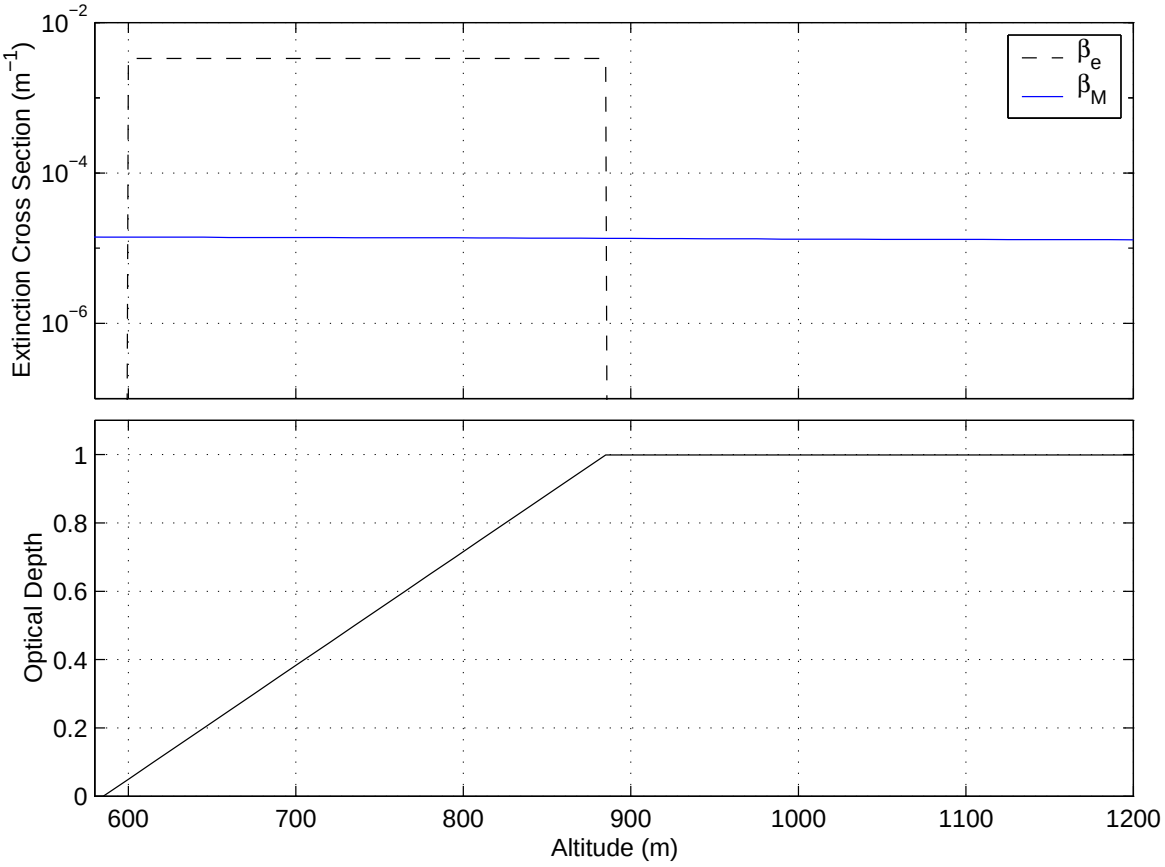


Figure 3.1 Model Cloud Optical Properties

At this time the Monte Carlo does not provide a measurement of the statistical fluctuations in the values of $P_n$.

The Monte Carlo, Gaussian, and infinite FOV model are in agreement (see figure 3.2). The infinite FOV deviates slightly from the Monte Carlo and the Gaussian models, because these models only approximate an infinite FOV with a value of 10.3 mrad. This is especially clear for 3rd and 4th order scattering, above 900 meters altitude. Figure 3.3 shows the ratios for three different fields of view. The plotted ratio is:

$$G(r) = \frac{P_2(r, fov_w) + P_3(r, fov_w) + P_4(r, fov_w)}{P_1(r, fov_n) + P_2(r, fov_n) + P_3(r, fov_n) + P_4(r, FOV_n)} \qquad [3.14]$$

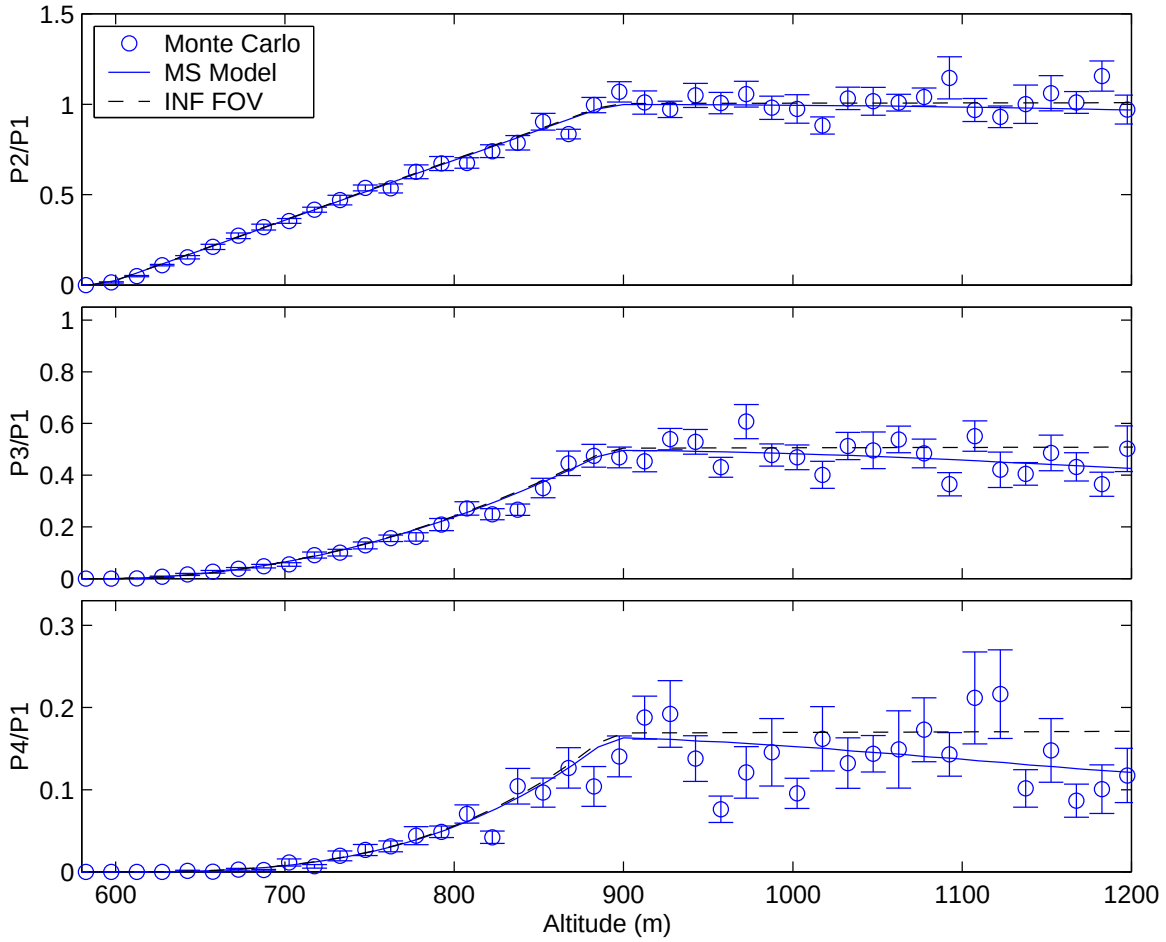


Figure 3.2 $P_n/P_1$, Gaussian Model - Monte Carlo Comparison (10.3mrad FOV)

Where $fov_w$ is the particular wide FOV, $fov_n$ is the narrowest receiver FOV. The multiple scatter contribution to $fov_n$ is small, so that this equation can be approximated by,

$$G(r) \approx \frac{P_2(r, fov_w) + P_3(r, fov_w) + P_4(r, fov_w)}{P_1(r, fov_n)} \qquad [3.15]$$

This comparison does not include the results from the infinite FOV model since the receiver FOV can longer be considered infinite. The 0.963 mrad , and 0.296 mrad results show a large decay in the multiple scattering contribution above the cloud top, this is due to the multiple scattered photons leaving these FOV. Even with the large number of photons collected, in this Monte Carlo run the 0.296 mrad FOV shows fairly poor statistics. However, a rough agreement

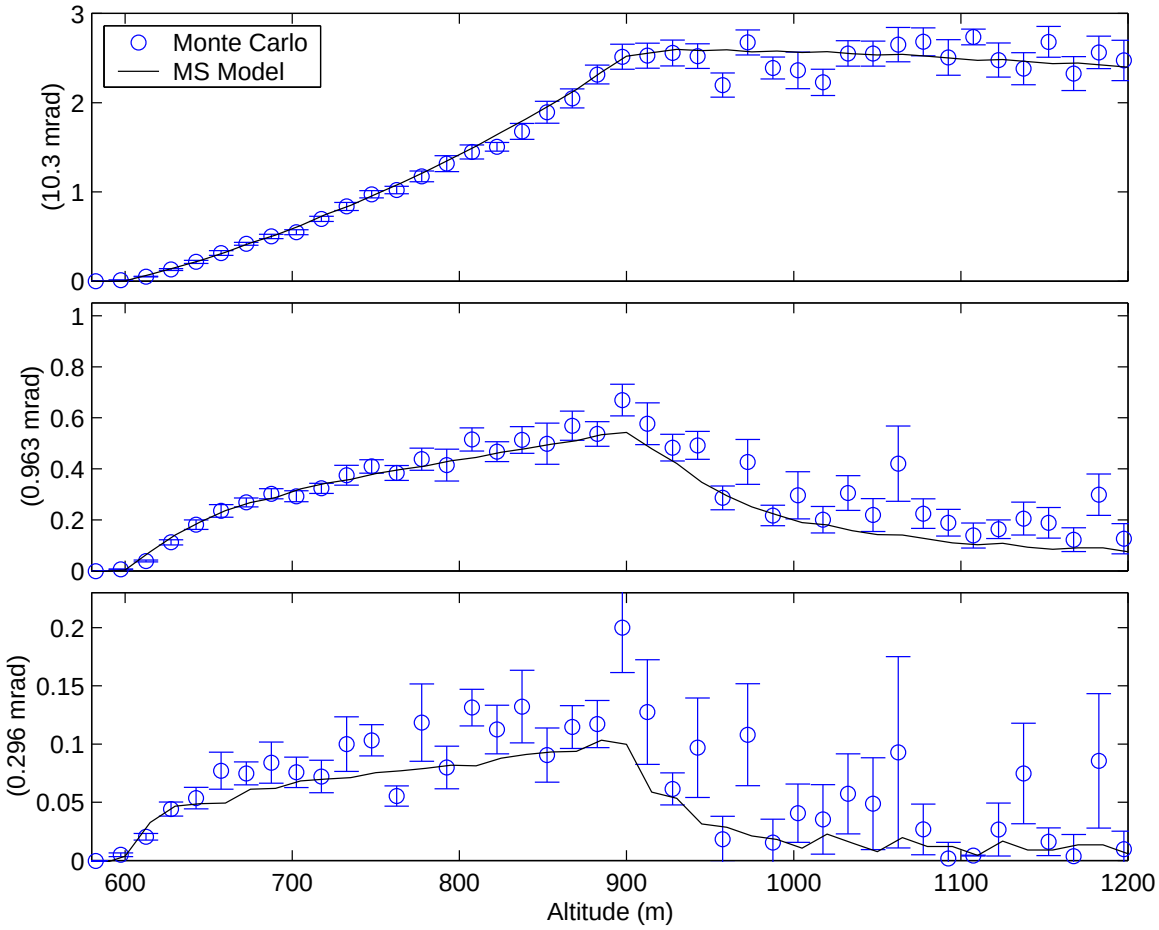


Figure 3.3 FOV Ratios,$(P_4 + P_3 + P_2)/P_1$ , Gaussian Model-Monte Carlo Comparison

between the two models can be seen. Also, the Gaussian model results are not smooth in this case because of roundoff error in the calculation of the multiple scatter contribution. So, these comparisons show that the Gaussian model can be used to determine the contribution of multiple scattering to the lidar signal.

# Chapter 4

# Measurement and Data Analysis Techniques

## 4.1 Introduction

Values of the effective radius, $a_e$, are inferred from the comparison of HSRL multiple scattering data and Gaussian model results, computed using different values of $a_e$. The HSRL provides profiles of the aerosol backscatter cross-section $\beta'_a(r)$, and extinction cross-section $\beta_e(r)$, as shown in section 2.3. Given these profiles the Gaussian model can be used to compute the multiple scatter contribution for different FOV and values of $a_e$. The HSRL also provides measurements of $M(r, fov)$, section 2 of this chapter discusses how this is accomplished. Section 3 then describes how the ratios $G(r)$ are computed from measurements of $M(r, fov)$ so they can be compared with the Gaussian model results of $G(r)$. The final section discusses how the HSRL profile of $G(r)$ must be corrected for the relative efficiency factor between the two detectors used to make single and multiple scattering measurements.

## 4.2 Measuring Multiple Scattered Photons: HSRL Receiver

This section describes features of the HSRL receiver required for multiple scattering measurements. Further details about the HSRL can be found in appendix A, and in (Piironen, 1994). Figure 4.1 shows a schematic of the HSRL receiver setup. The receiver is split into two major parts, the narrow field of view (NFOV) channels, and the annular wide field-of-view (AWFOV) channels. The NFOV channels measure the single scatter lidar return, which are used to derive the quantities of $\beta'_a(r)$, $\tau(r)$ and $\delta$. This FOV is designed to be as small as possible to minimize the contribution from multiple scattered photons. The NFOV minimum size

is limited by the laser transmitter divergence, since the FOV must be large enough to collect a large percentage of the single scattered return. Currently, the laser transmits with a Gaussian beam profile with a divergence of 110 $\mu$rad, full-angle $e^{-1}$ width. The NFOV size is currently set to 110 $\mu$rad.

The FOV of the HSRL is controlled by an aperture placed at the focal plane of the telescope. This is because an incoming photon with angle $\theta$ with respect to the optical axis of the telescope will be mapped to a position, $y$, on the focal plane. The relationship is expressed mathematically as, $y \sim f \cdot \theta$, where f is the effective focal length of the telescope (figure B.1). The limiting aperture for the NFOV is shown in figure 4.1 and in an expanded view in figure 4.2, the location of the aperture is in fact at an image of the telescope prime focus. The NFOV aperture is an 800 $\mu m$ hole in center of a flat mirror. Photons that fall outside the NFOV are redirected by the mirror to the AWFOV channels. This allows both normal HSRL and multiple scattering measurements to be made simultaneously with a minimum amount of signal loss (i.e. as opposed to splitting the entire signal off before the NFOV aperture.)

The AWFOV aperture is placed at an image of the telescope prime focus before the NFOV aperture. This aperture can be changed in diameter and is controlled by the data acquisition system. Typically the aperture diameter is changed after every averaging period. One averaging period or *shot* is the sum of 4000 individual *seeded* laser pulses. *Seeded* laser pulses are those that have the proper spectral characteristics necessary to separate the HSRL signal for aerosol and molecular scattering. During operation the laser is typically seeded 70% of the time, fired at a rate of $4kHz$. Each laser *shot* takes approximately 3 seconds to acquire. The AWFOV aperture is stepped every shot through a cycle of 3 to 4 different diameters/FOVs (i.e. 0.3, 0.5, 1.0, 2.0, 0.3, 0.5... $m$rad). This is done to simplify data analysis and to minimize the time between observations with each AWFOV.

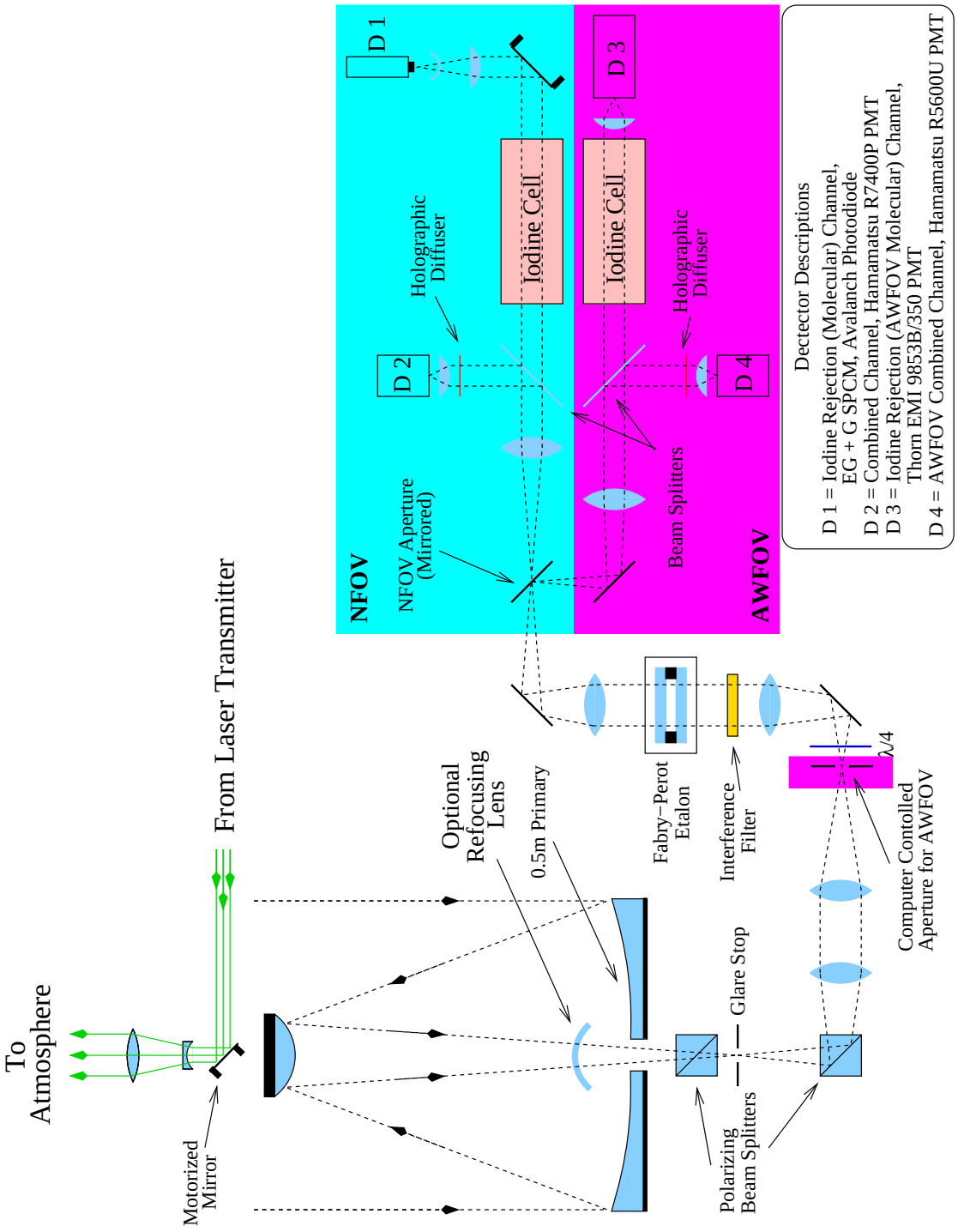


Figure 4.1 A diagram of the HSRL receiver

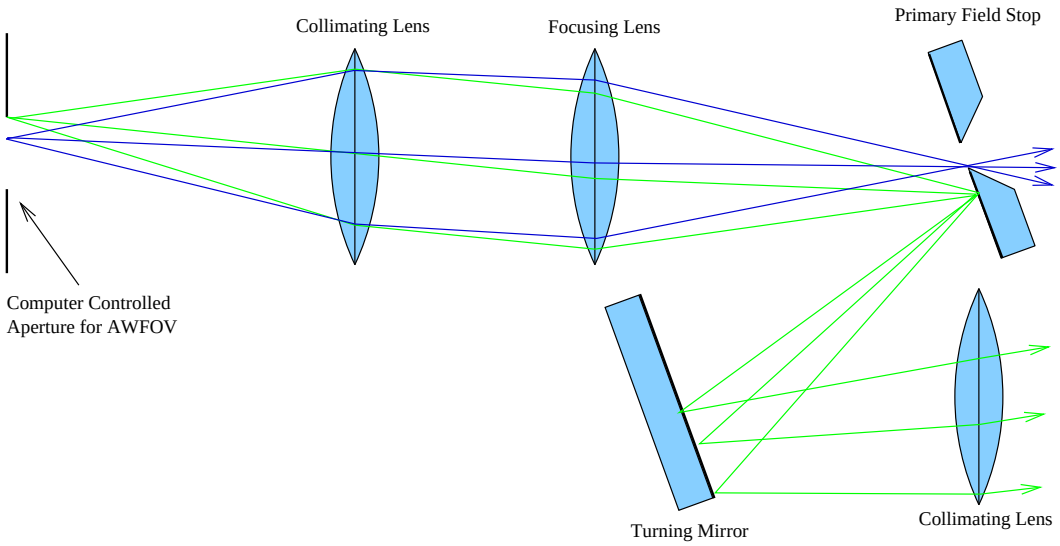


Figure 4.2 A ray diagram of the primary field stop and how it separates the narrow field of view from wider fields of view. The rays represent possible paths of photons that scattered back to the receiver from outside(green) or inside(blue) the NFOV. NFOV.

## 4.3 Deriving the AWFOV Ratio Equation

This section describes how the ratios $G(r)$ are computed from measurements of $M(r, fov)$ so they can be compared with the Gaussian model results of $G(r)$. The following two equations describe the lidar signals measured with the AWFOV molecular channel, and the narrow molecular FOV channels, respectively.

$$N_\Psi(r) = \Big((e_\rho - e_\theta) + M_\Psi(r)\Big)R(r)C_\Psi \quad [4.1]$$

$$N_\theta(r) = \Big(e_\theta + M_\theta(r)\Big)R(r)C_\theta \quad [4.2]$$

where

$N_\Psi(r)$ = the number of photons received in the wide annular FOV as a function of range. This is a measured quantity.

$N_\theta(r)$ = the number of photons received in the narrow FOV channel as a function of range. This is a measured quantity.

$\Psi$ = $\rho - \theta$,the full-angle receiver AWFOV.

$e_\theta$ = $(1 - exp(-\theta^2/\theta_t)^2)$ the percentage of energy transmitted within the FOV $\theta$. $\theta_t$ is the transmitter divergence full-angle $e^{-1}$ width.

$e_\rho$ = the percentage of energy transmitted within the FOV $\rho$.

$R(r)$ = $N_o \dfrac{cA}{2r^2}\Big(\dfrac{3}{8\pi}\beta_m(r)\Big)e^{-2\tau(r)}$ [4.3]
The total Rayleigh component of the signal, including aerosol extinction and range dependence.

$N_o$ = the number of transmitted photons.

$M_\Psi(r)$ = the signal from aerosol multiple scattering in the wide annular FOV $\Psi$. Defined as a percentage of the total Rayleigh signal.

$M_\theta(r)$ = the signal from aerosol multiple scattering in the narrow FOV $\theta$.

Defined as a percentage of the total Rayleigh signal.

$C_\Psi$ = annular-wide FOV detector efficiency and optical transmission factor.

$C_\theta$ = narrow FOV detector efficiency and optical transmission factor.

If the we use the lidar signals from a region where there is little or no aerosol single or multiple scattering a constant $k$ can be defined as:

$$k = \frac{N_\Psi(r_{mol})}{N_\theta(r_{mol})} = \frac{(e_\rho - e_\theta)R(r)C_\Psi}{e_\theta R(r)C_\theta} = \frac{(e_\rho - e_\theta)C_\Psi}{e_\theta C_\theta} \quad [4.4]$$

The ratios G(r) are calculated using a form of the following equation. This form was chosen to minimize the contribution from single scattering in the annular FOV.

$$G(r) = \frac{N_\Psi(r) - kN_\theta(r)}{N_\theta(r)} \quad [4.5]$$

By expanding this equation it can be seen that the single scattered component is removed from the numerator.

$$\begin{aligned} G(r) &= \frac{((e_\rho - e_\theta) + M_\Psi(r))R(r)C_\Psi - k(e_\theta + M_\theta(r))R(r)C_\theta}{(e_\theta + M_\theta(r))R(r)C_\theta} \\ &= \frac{((e_\rho - e_\theta) + M_\Psi(r))C_\Psi - \frac{(e_\rho - e_\theta)C_\Psi(e_\theta + M_\theta(r))C_\theta}{e_\theta C_\theta}}{(e_\theta + M_\theta(r))C_\theta} \\ &= \frac{(M_\Psi(r) - (e_\rho - e_\theta)M_\theta(r))C_\Psi}{(e_\theta + M_\theta(r))C_\theta} \end{aligned} \quad [4.6]$$

The ratios must be corrected for the term $C_\Psi/C_\theta$, the relative detector and optical transmission factor. This can be computed by inverting the equation used to determine $k$ and its computed value.

$$\frac{C_\Psi}{C_\theta} = \frac{ke_\theta}{(e_\rho - e_\theta)} \quad [4.7]$$

Note that the transmitter divergence, $\theta_t$ and the receiver FOV, $\theta$ and $\rho$, must also be used to calculate this ratio. Finally, the computed ratios are:

$$G'(r) = \frac{G(r)}{\frac{C_\Psi}{C_\theta}} = \frac{N_\Psi(r) - kN_\theta(r)}{N_\theta(r)}\left(\frac{C_\theta}{C_\Psi}\right) \quad [4.8]$$

## 4.4 Correcting for the Relative Detector Efficiencies

The HSRL AWFOV ratios must be properly scaled by the relative detector efficiency and optical transmission factor, which is expressed as a single quantity, the relative channel efficiency. It is impractical to measure the channel efficiencies directly, so the relative efficiency is measured instead.

### 4.4.1 Method I

The first method is to use the equation 4.7. The value of $k$ is calculated from equation 4.4, $k = N_\Psi(r)/N_\theta(r)$, from lidar measurements in a region absent of aerosol scattering. The transmitter beam divergence has been estimated from measurements to have a Gaussian profile containing 88% of the total energy with a divergence of $110 \pm 10\mu$rad. Using this value for the transmitter divergence and a NFOV width of 110$\mu$rad, the relative channel efficiency factor $C'$ is calculated to be $0.34 \pm 0.10$.

### 4.4.2 Method II

The second method uses information only collected from the calibration source. The calibration source is an aperture designed to uniformly illuminate the AWFOV and NFOV apertures[1]. The signal measured from the calibration source is proportional to the aperture area and the channel efficiencies. This method assumes that the calibration source is uniformly illuminated, and that all optical elements in the HSRL receiver have been correctly aligned.

$$C' = \frac{S_{\rho-\theta}}{S_\theta} \frac{A_\theta}{(A_\rho - A_\theta)} \qquad [4.9]$$

Where $A_\theta$ is the area of the narrow FOV aperture imaged onto the AWFOV aperture, and $A_\rho$ is the area of the annular wide field of view aperture. The value of $C'$ measured with this technique is $0.31 \pm 0.09$.

[1] See Piironen (1994) for further information about the calibration source

### 4.4.3 Method III

The final and preferred method to correct for the relative channel efficiency does not depend on system calibrations. From the infinite FOV model, equation 3.3, no longer depends on $\langle\theta_s\rangle$ which is proportional to $a_e$. So for ranges in the cloud where $r \gg (r - r_c)$, the ratio $(P_4 + P_3 + P_2)/P_1$ is independent of $a_e$. So the ratio $G(r)$ computed from HSRL measurements should have the same slope if the correct value of $C'$ is used. In this case $C'$ was varied until $G(r)$ has the same slope as $(P_4 + P_3 + P_2)/P_1$. As long as at least one receiver FOV is large compared to $\langle\theta_s\rangle$, this relationship can be used. Figure 5.5, the 2200 $\mu$rad FOV panel, demonstrates this effect. These are the Gaussian model results computed from the extinction measurements on February 22, 2001, as a function of $a_e$. Once the multiple scattering equilibrium is obtained a few hundred meters from cloud base, all the ratios have the same slope. Since this FOV is not infinite, at farther ranges the multiple scatter signal decays as photons exit the FOV.

The value of $C'$ found to give the best fit slope to the model results from 2/22/01, is 0.35. This is within the limits of experimental error in $C'$ computed using both methods I, and II above.

# Chapter 5

# Results

## 5.1 February 22, 2001 Measurements

On February 22, 2001 the HSRL collected data from 01:14 UT until 04:53 UT, in Madison, Wisconsin (43.07 N, 89.38W). During this period the AWFOV aperture was operated to collect multiple scattering data. High altitude ice clouds (cirrus) were observed during this period. Figure 5.1 shows altitude versus time image of aerosol backscatter cross-section $(\beta'_a(r))$ derived from inverted HSRL data. Figure 5.2 shows and altitude versus time image from the same period of inverted aerosol depolarization.

Since the multipley scattered signal measured with the HSRL is quite small, the data must be averaged to ensure that the statistical errors (photon counting) are small. In this case 24 minutes, 400 laser shots, were required to reduce statistical errors to an acceptable level. Since four AWFOVs were used the total number of shots summed for each channel was 100. The averaging period was from 02:17:36 until 02:41:22 UT. During this period the cloud base remained relatively constant and uniform. Also, the region below the cloud layer was free from other cloud layers or aerosols.

Multiple scatter calculations require the atmospheric profile of $\beta_a(r)$. Since the maximum optical depth of this section of the cloud was 0.7, it was possible to calculate $\beta_a(r)$ from equation 2.9. Figure 2.2 (shown previously) is a plot of the simple optical depth, $\tau_s(r)$, and the integrated extinction, $\beta_a(r)$, calculated using $\langle P_a(\pi)/4\pi\rangle = 0.027$.

Although the errors in $\beta_a(r)$ were not determined explicitly, the errors in $\beta'_a(r)$ and $\tau_s$ were calculated to illustrate the largest possible sources of error in $\beta_a(r)$. Figure 5.3 shows

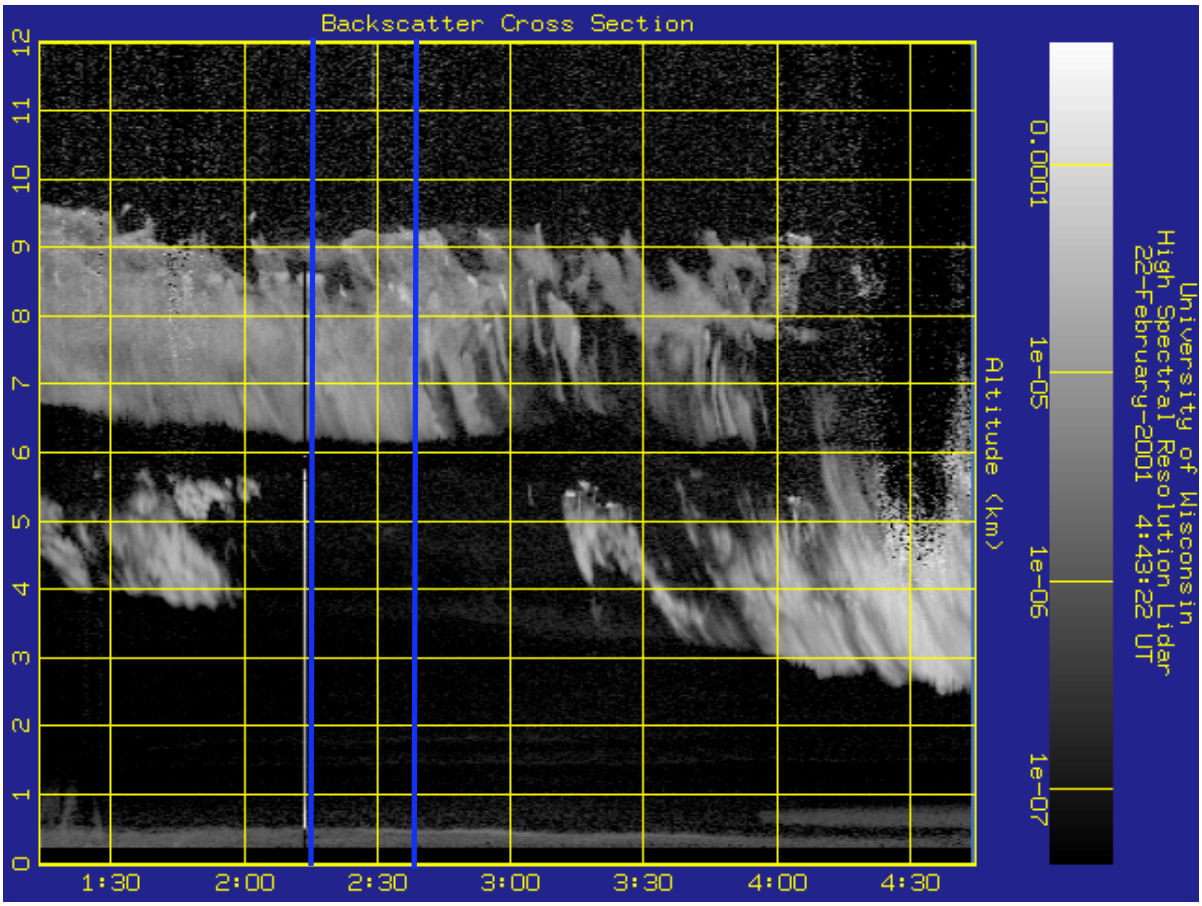


Figure 5.1 02/22/2001, Altitude vs. time image of aerosol backscatter cross-section showing cirrus clouds from 01:14 to 04:53 UT. The period used to estimate the effective particle size is from 02:17:36 to 02:41:22 UT. This area is delineated by vertical blue lines.

the derived profile of $\beta'_a(r)$ and the associated statistical errors. Figure 5.4 shows $\tau_s$, as well as the contribution of both statistical errors and errors from using a atmospheric temperature profile that may not be representative of the atmospheric temperature profile over Madison, WI, during the HSRL operation. During normal HSRL operations radio sonde profiles from Green Bay, WI are used for temperature and density information. A difference between the true vertical lapse rate through the cloud layer, and the lapse rate of the temperature profile used to calculate the theoretical molecular profile, $N_T(r)$, is a significant source of error for the simple optical depth, $\tau_s(r)$. A constant difference between the true temperature profile and

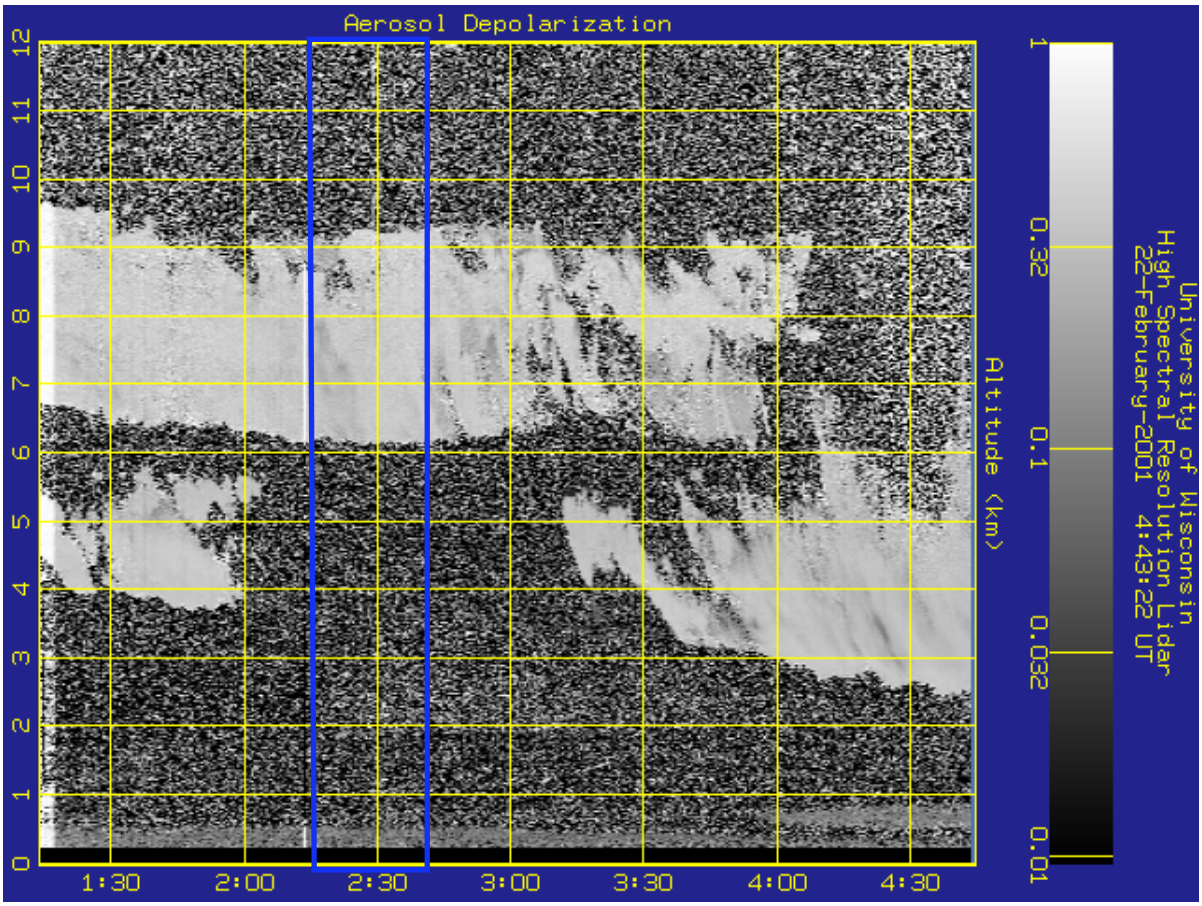


Figure 5.2 02/22/2001, Altitude vs. time image of aerosol depolarization, from 01:14 to 04:53 UT. The values of depolarization, ($\approx 0.4$), indicate that the cloud consists of ice particles for the entire period, 01:14 to 04:53 UT. The period used to estimate the effective particle size is from 02:17:36 to 02:41:22 UT. This area is delineated by vertical blue lines.

the one used to calculate $N_T(r)$ is *not* a significant source of error since $N_T(r)$ is scaled to the measured molecular signal at reference altitude below the cloud.

The error in the lapse rate was estimated by computing the maximum difference in the lapse rates between 6 and 10 km, from the three different soundings. The maximum difference was determined to be $1^{\circ}$/km. When including both the statistical and lapse rate errors, the error in the simple optical depth was less than 3% at 12 km. This is the reference altitude used to determine the profile of integrated aerosol extinction.

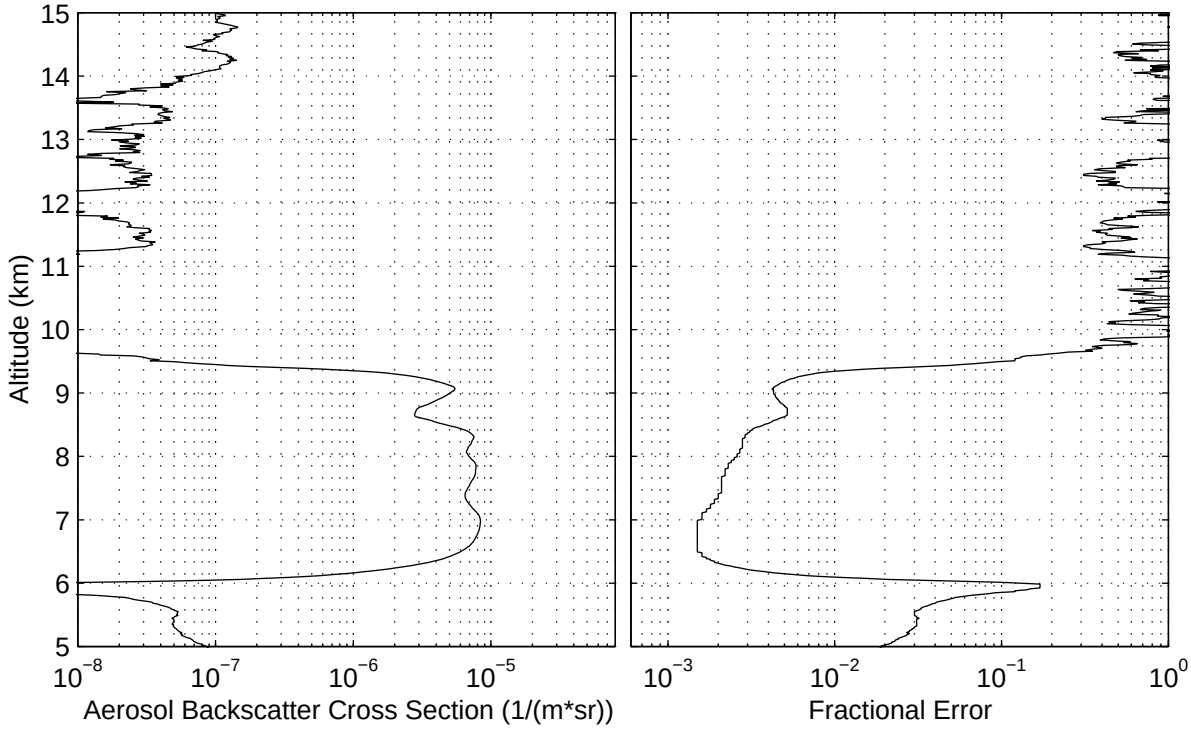


Figure 5.3 02/22/2001, mean cirrus backscatter cross section and statistical errors for the period 02:17:36 to 02:41:22 UT.

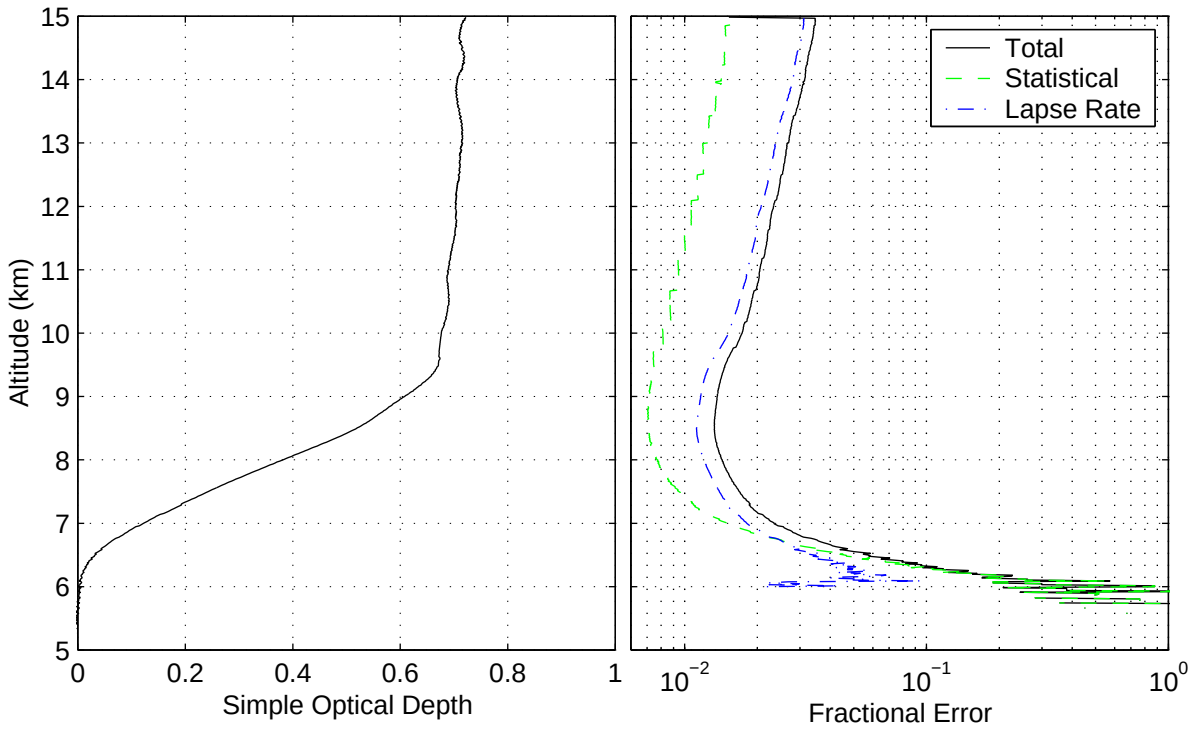


Figure 5.4 02/22/01, mean simple optical depth and fractional errors for the period 02:17:36 to 02:41:2 UT. The errors shown are from photon counting (statistical) errors and from errors due to using a atmospheric temperature profile that may not be representative of the temperature profile over Madison, WI, during the HSRL data collection.

## 5.2 Gaussian Model Results

The multiple scatter model was run with the parameters given in table 5.2. The 84 separate data files (1 for each FOV and particle size) required 8 hours to complete running 2 processes on the computer describe by Table A.

Table 5.1 Multiple Scatter Model Parameters for 02/22/2001, 02:17-02:41 UT.

| | |
|---|---|
| Transmitter Div. | 110 $\mu$rad |
| Receiver FOV (narrow) | 110 $\mu$rad |
| (Annular wide 1) | 296 $\mu$rad |
| (Annular wide 2) | 503 $\mu$rad |
| (Annular wide 3) | 963 $\mu$rad |
| (Annular wide 4) | 2200 $\mu$rad |
| (Annular wide 5) | 10.3 $m$rad |
| $a_e(r)$ | uniform in altitude, 40..5..110 $\mu$m |
| $\beta_m(r)$ | Green Bay, WI, 00:00 UT Sounding. |
| $\beta_a(r)$ | Values computed from section 5.1. |
| Max scattering order | 4 |

The results from this model run are summarized by figure 5.5. This figure shows the AWFOV ratios, $G(r)$, for each FOV as described in section 4.3 by equation 4.8. Its purpose is to demonstrate the variability of the AWFOV ratios with both particle size and FOV. The first thing to note is that for a given value of effective particle size the maximum value of the ratio $G(r)$ decreases with smaller FOVs. This is because with each scattering event the probability that a photon will leave a given FOV increases. So, large FOVs contain more photons of higher scattering order than small ones.

By just considering one FOV, the smaller particles always have the smallest peak value in $G(r)$. Since the diffraction peak width is inversely proportional to the effective particle size,

the smaller particles have the broadest diffraction peak. This limits the highest scattering order that contributes to the multiple scatter signal.

Near cloud base and for large receiver FOVs the differences between $G(r)$ for different particle sizes are smaller. First, near cloud base only the first few scattering orders are significant, there has not been enough space for the photons to scatter more than a few times. So, the dependence on the diffraction peak width is small. As the receiver FOV increases the region where multiple scattering is insensitive to particle size becomes larger. Even though photons that have scattered many times contribute to the signal, they are all still contained within the receiver FOV so the dependence on the diffraction peak width is small. This leads to the infinite FOV case where there is no dependence on particle size inside the cloud. However, at higher altitudes, in this case near cloud top, the term $r/(r - r_c)$ from equation 3.2 becomes smaller, and $An < 1$, so, a significant variation in the profiles $G(r)$ with effective particle size is observed.

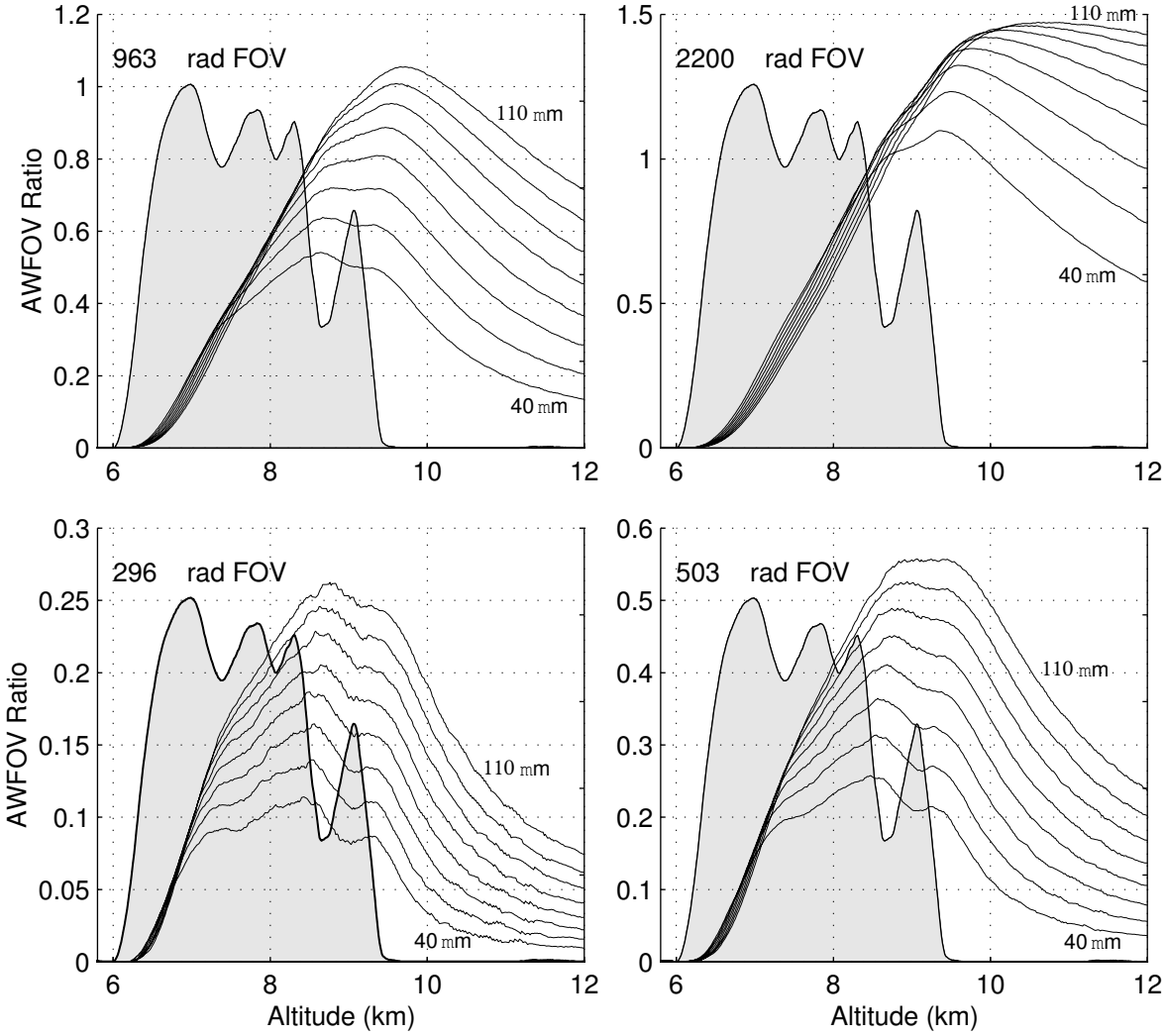


Figure 5.5 02/22/2001, 02:17:36-02:41:2 UT, Gaussian model AWFOV ratios, $G(r)$, for each FOV and particle sizes ranging from 40-110 $\mu$m in intervals of 10 $\mu$m. The shaded area is the profile of $\beta'_a(r)$, shown for reference. $\beta'_a(r)$ is plotted on a linear scale ranging from $0$ to $1.0 \cdot 10^{-5}$ $(m^{-1} \cdot sr^{-1})$.

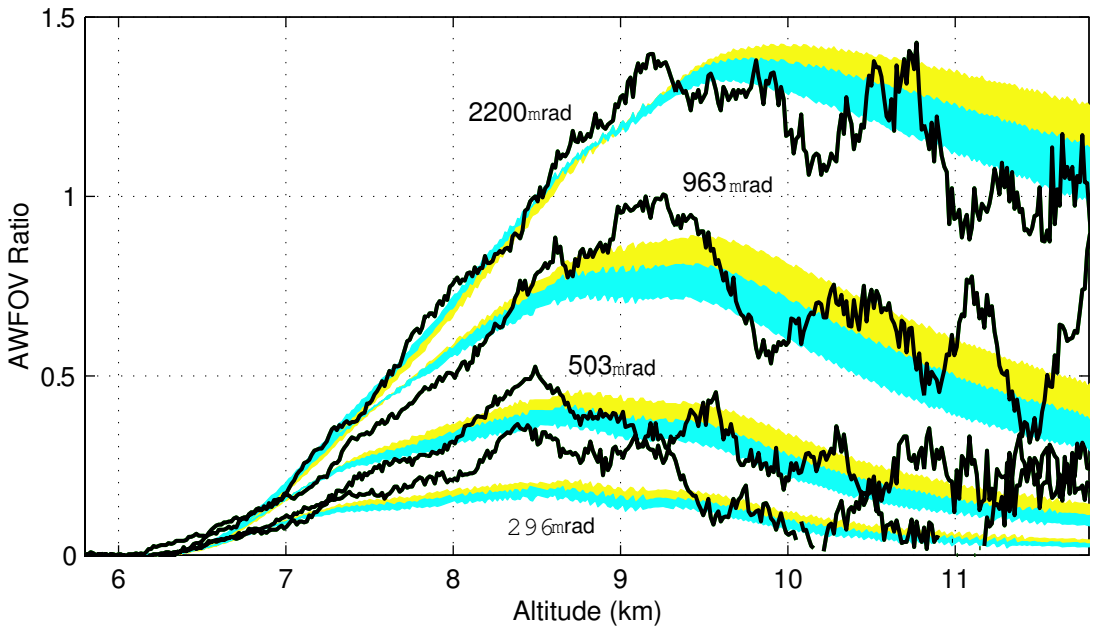


Figure 5.6 02/22/2001, 02:17:36-02:41:2 UT, $G'(r)$ for all FOV, model and HSRL results comparison. The cyan and yellow shaded curves represent the approximate model results. For the cyan curve, $a_e$ ranges from 60 to 70 $\mu$m. For the yellow curve, $a_e$ ranges from 70 to 80 $\mu$m. The HSRL derived ratios (solid lines) are plotted at a vertical resolution of $15m$, and were smoothed with a 21 bin $(315m)$ moving average filter.

## 5.3 Determining the effective radius

The average effective radius can be determined by comparing the real AWFOV to those computed with the multiple scatter model. The method is to find the set of computed AWFOV ratios, $G(r)$, that best fit the data for each FOV for only one effective radius, or range of effective particle radii.

The average value of $a_e$ during the period 02:17:22-02:41:36 UT was determined to be $70\mu$m. This is based on the comparison of the approximate and HSRL values of $G'(r)$ shown in figure 5.6. The HSRL ratios for each FOV along with a shaded curve computed from the Gaussian model, are shown in this figure. Each shaded curve represents a range of $a_e$ from $60 - 80\mu$m, for each FOV. The HSRL values of $G'(r)$, were calculated according to equation 4.8, using a value for $C'$ of 0.35, as discussed in section 4.4.3.

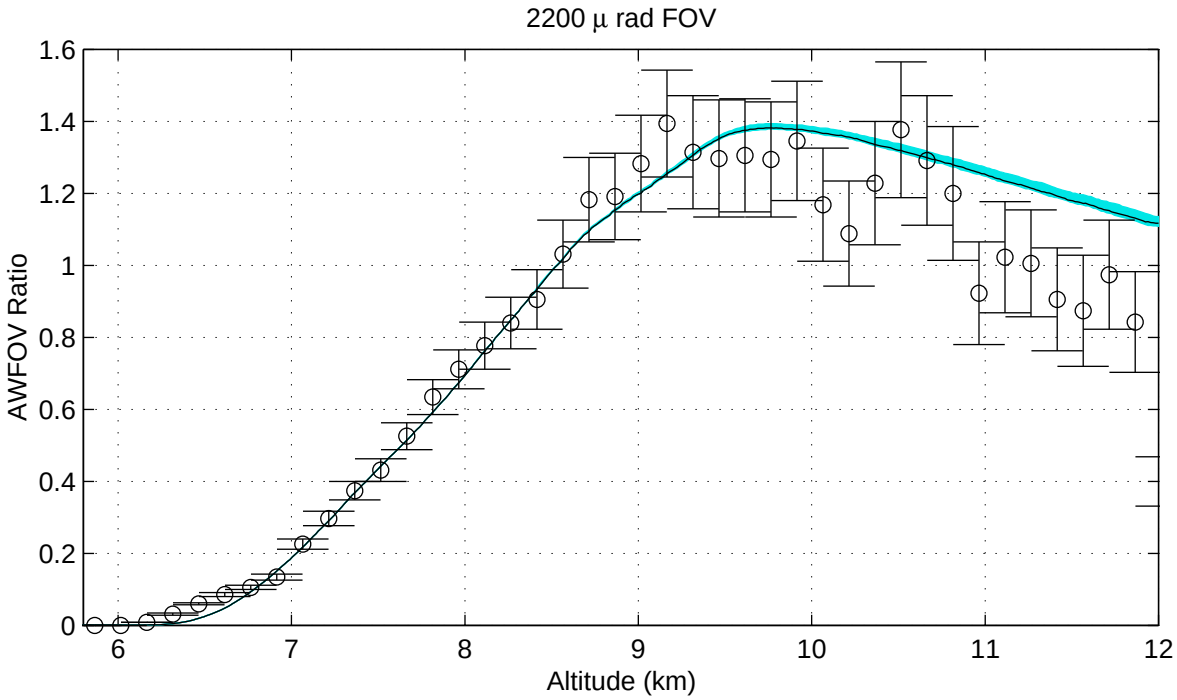


Figure 5.7 02/22/2001, 02:17:36-02:4136 UT: AWFOV ratios results for $2200\mu rad$, HSRL derived values $(\circ)$, with error bars representing statistical errors. The approximate model results are shown by the solid line, and shaded area. The shaded area represents the range of model results $\pm$ 30 $\mu$rad for the specified receiver AWFOV.

The figures 5.7 through 5.9 show the comparisons of $G'(r)$, $a_e = 70$ $\mu$m, from the Gaussian model with the HSRL data. The uncertainty in the measurement of the diameter of the computer controlled aperture is approximately 0.15 mm. This can be translated directly into an error in the size of the AWFOV, which is $\pm 30$ $\mu$rad. So, for each AWFOV, the ratios $G'(r)$ have been calculated with the Gaussian model to show the dependence of $G'(r)$ on this uncertainty. The shaded area in these figures represent the variation in $G'(r)$ for the error in the measurement of the size of the AWFOV apertures.

Also, the HSRL derived values of $G'(r)$ are displayed with error bars that represent the uncertainty from statistical errors. It is important to note that these error bars do not account for the variance seen between neighboring points at altitudes above $9km$. At this time it is unclear why the fluctuations in $G'(r)$ above $9km$ are so large.

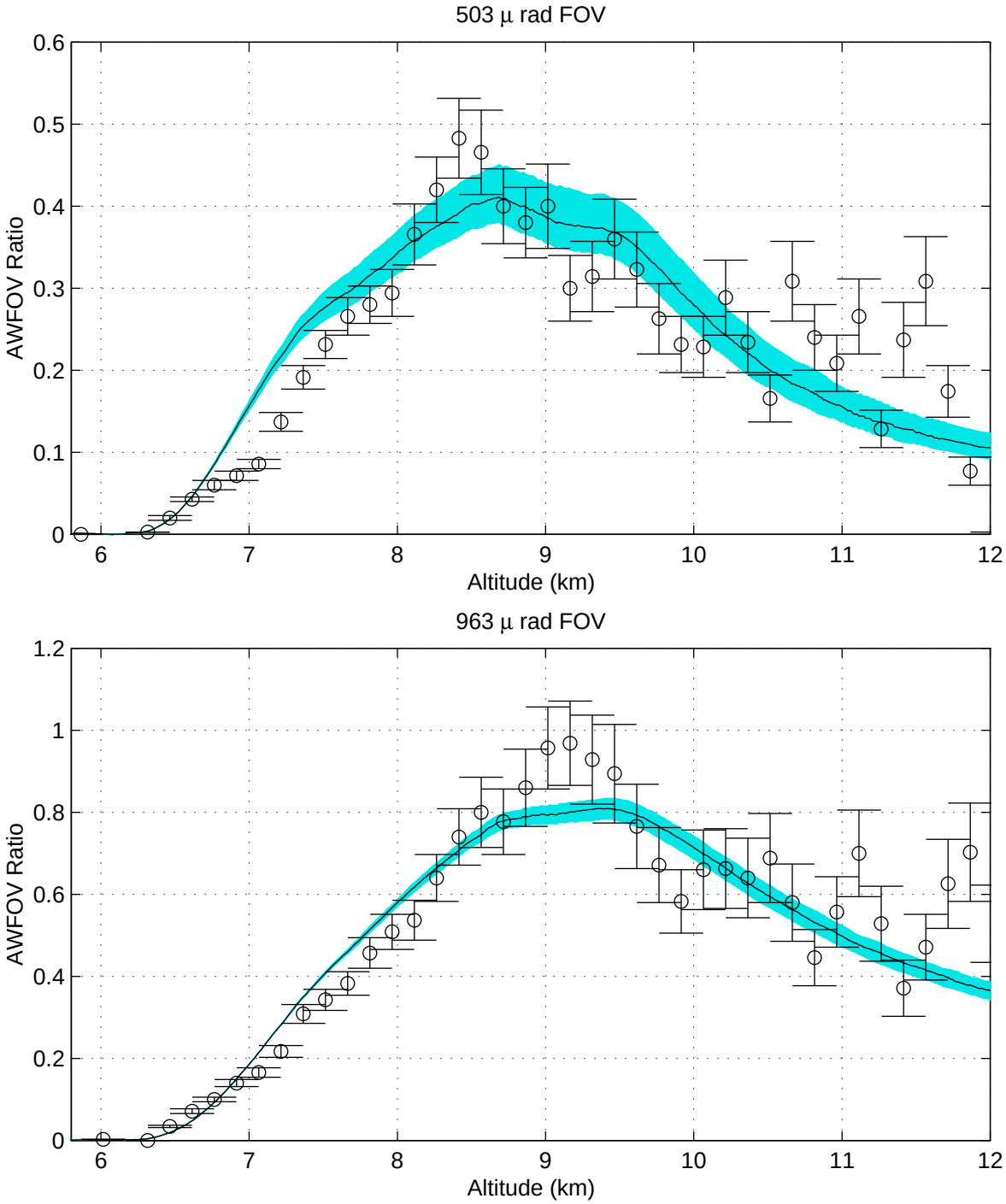


Figure 5.8 02/22/2001, 02:17:36-02:4136 UT: AWFOV ratios results for $503\mu$rad (top), and $963\mu$rad (bottom) FOVs. HSRL derived values $(\circ)$, with error bars representing statistical errors. The approximate model results are shown by the solid line, and shaded area. The shaded area represents the range of model results $\pm$ 30 $\mu$rad for the specified receiver AWFOV.

In general the results from the three larger AWFOVs comparisons show much better agreement. However, if the comparisons are examined one FOV at a time significant discrepancies are evident. For both the 503 and the 963 $\mu$rad FOVs the approximate model values of $G(r)$ between 7 and 8 km are 15% to 100% greater than the HSRL values in the same region, see figure 5.8. This is inconsistent with the 2200 $\mu$rad FOV comparison at the same altitudes where the differences on average are only a few percent, see figure 5.7. Another disagreement is seen in the 2200 $\mu$rad AWFOV ratio comparison. This comparison indicates that at altitudes above 9 km the approximate model data would fit better with a smaller effective particle size or AWFOV. This is contradictory however, to the comparisons of the 503 and 963 $\mu$rad FOVs where a smaller particle size would produce an AWFOV ratio that is to low above 9 km.

The largest discrepancy between the approximate model results and the HSRL computed ratios are seen in the smallest AWFOV (296 $\mu$rad), see figure 5.9. This discrepancy however, can be explained as a systematic error in the measurement of the 296 $\mu$rad AWFOV signal. In the current measurement configuration the computer controlled aperture is stepped in the following order (1.33, 2.27, 4.34, 10.04, 1.33, 2.27, ...$etc$ ($mm$)). Each aperture is held for 1 shot, $\approx$ 2 seconds. The transition from the largest to the smallest aperture takes approximately 500 $ms$ to complete. So the $296\mu$rad signal includes photons from larger fields-of-view, causing the ratio to be larger than expected.

With the exception of the 296 $\mu$rad AWFOV results, the discrepancies seen in the remaining wider FOVs are not unexpected. Especially considering the assumptions that have been made. It was assumed that $n(a)$ and $\mathcal{P}(\pi)$ remain constant with altitude and throughout the averaging period. Heymsfield and Iaquinta (2000) have shown for midlatitude clouds that it would be likely to find larger particles near cloud base since the larger particles have a greater fall velocity. This could possibly explain the results from the 503 and 963 $\mu$rad FOVs between 7 and 8 km. If a few large particles were present in this region, the narrower diffraction peak would keep more photons in the NFOV, resulting in a smaller ratio in that region.

Variations of the cloud extinction with respect to time are manifested as an uncertainties in the measured extinction profile and the measured multiple scattering signal, $M(r, fov)$.

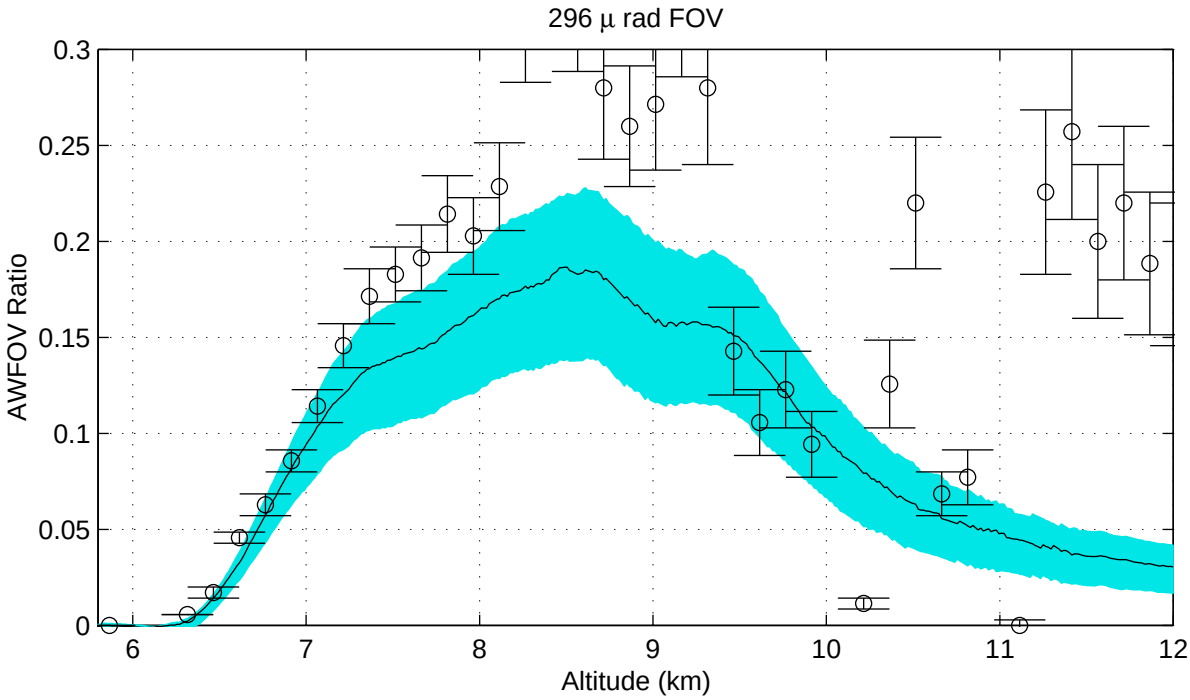


Figure 5.9 02/22/2001, 02:17:36-02:4136 UT: AWFOV ratios results for $296\mu rad$, HSRL derived values $(\circ)$, with error bars representing statistical errors. The approximate model results are shown by the solid line, and shaded area. The shaded area represents the range of model results $\pm$ 30 $\mu$rad for the specified receiver AWFOV.

Since $M(r, fov)$ depends on $exp(+\tau(r))$, and the molecular signal, $N_m(r)$, on $exp(-\tau(r))$, the measurements of $M(r, fov)$ and $\tau_s(r)$ respond differently when the data is averaged over time. The profile of $M(r, fov)$ will be dominated by temporal sections of the cloud that were optically dense compared to the mean optical depth. $\tau_s(r)$ will be dominated by temporal sections that were optically thin, compared to the mean optical depth. So, the uncertainty in both $M(r, fov)$ and $\tau_s(r)$ can be minimized by shortening the averaging time, or by selecting a temporal section of the cloud where the optical depth remained relatively constant. At this time a quantitative analysis of the magnitude of this uncertainty has not been done. It is estimated that temporal section of the cloud used in this presentation is uniform enough that uncertainties due to temporal averaging are no more than those of the statistical and AWFOV size uncertainties.

# Chapter 6

# Summary

This thesis has presented a method of determining the effective particle size from lidar multiple scattering measurements, with the University of Wisconsin High Spectral Resolution Lidar. Specifically, the multiple scattered signal is measured that consists of photons that have only backscattered from molecules. Using simultaneous measurements of extinction provided by the HSRL, an approximate analytical solution to lidar multiple scattering is used to generate the multiple scattering contribution as a function of $a_e$, $\langle \mathcal{P}(\pi) \rangle$, and $\mathcal{P}(\pi)$. Since the backscattering particles are molecules the backscatter phase function information is provided by Rayleigh scattering theory. The solution for $\langle \mathcal{P}(\pi) \rangle$ is in fact trivial since molecular scattering is isotropic for scattering angles near $\pi$. The model results are then compared to the HSRL measurements. When the model and measurements agree, the value of the effective particle size is assumed to represent that of the cloud. Currently, multiple scatter measurements are limited to nighttime operations.

For the case on February 22, 2001, the first successful molecular multiple scatter measurements were made. Using the extinction profile derived from HSRL measurements, the Gaussian multiple scatter model results indicate that the cloud $a_e$ was 70 $\pm$ 10$\mu$m. This is a plausible value for $a_e$ for cirrus clouds. It was assumed that particle size distribution and hence $a_e$ do not vary with height. The optical depth and effective particle size are assumed to remain constant with time over the averaging period. In this case the temporal section of the cloud was chosen based on its uniformity, so that good signal-to-noise values could be obtained in the annular wide FOV channels without introducing large uncertainties from averaging over inhomogeneities in the cloud.

Future improvements to this technique will include, resolving the range dependence of $a_e$, and calculating the multiple scatter contribution using a gamma size distribution. Also, a better evaluation of the measurement uncertainties, such as the transmitter beam shape and divergence, and the annular wide FOV aperture sizes, will be conducted. Further hardware improvements may include replacing the Molecular annular wide FOV detector will a detector that has a higher photon detection efficiency. This would reduce the temporal averaging time required to obtain good photon counting statistics.

# References

Allen, R. J. and C. M. R. Platt: 1977, Lidar for multiple backscattering and depolarization observations. *Appl. Opt.*, **16**, 3193–3199.

Benayahu, Y., A. Ben-David, S. Fastig, and A. Cohen: 1995, Cloud-droplet-size distribution from lidar multiple-scattering measurements. *Appl. Opt.*, **34**, 1569–1577.

Bissonnette, L. R.: 1996, Multiple-scattering lidar equation. *Appl. Opt.*, **35**, 6449–6465.

Bissonnette, L. R. and D. L. Hutt: 1995, Multiply scattered aerosol lidar returns: inversion method and comparison with in situ measurements. *Appl. Opt.*, **34**, 6959–6975.

Deirmendjian, D.: 1969, *Electromagnetic Scattering on Spherical Polydisperions*. Elsevier, New York.

Eloranta, E. W.: 1967, *An Investigation of Lidar Pulses Doubley Scattered by Atmospheric Aerosols*. Master's thesis, University of Wisconsin.

— 1972, *Calculation of Doubly Scattered Lidar Returns*. Ph.D. thesis, University of Wisconsin.

— 1998, Practical model for the calculation of multiply scattered lidar returns. *Appl. Opt.*, **37**, 2464–2472.

Eloranta, E. W. and S. T. Shipley: 1982, A solution for multiple scattering. *Atmospheric Aerosols: Their Formation, Optical Properties, and Effects.*, A. Deepak, ed., Spectrum, Hampton, VA, 227–239.

Grund, C. J.: 1987, *Measurement of Cirrus Cloud Optical Properties by High Spectral Resolution Lidar*. Ph.D. thesis, University of Wisconsin, Madison.

Hartmann, D. L., M. E. Ockert-Bell, and M. L. Michelsen: 1992, The effect of cloud type on the earth's energy balance: Global analyis. *J. Climate*, **5**, 1281–1304.

Heymsfield, A. J. and J. Iaquinta: 2000, Cirrus crystal terminal velocities. *J. Atmos. Sci.*, **57**, 916–938.

Lindzen, R. S., M. Chou, and A. Y. Hou: 2000, Does the earth have an adaptive infrared iris. *Bull Amer. Meteor. Soc.*, **82**, 417–432.

Liou, K.-N. and R. M. Schotland: 1971, Multiple backscattering and depolarization from water clouds for a pulsed lidar system. *J. Atmos. Sci.*, **28**, 772–784.

Measures, R. M.: 1988, *Laser Remote Chemical Analysis*. Wiley Interscience, New York.

Mishchenko, M. I., J. W. Hovenier, and L. D. Travis, eds.: 2000, *Light Scattering by Nonspherical Particles*. Academic Press, San Diego, CA, theory, Measurements and Applications.

Mitev, V. M., I. Grigorov, and V. B. Simenov: 1992, Lidar measurements of atmospheric aerosol extinction profiles: a comparison between two techniques-Klett inversion and pure rotational Raman scattering nethods. *Appl. Opt.*, **31**, 6469–6474.

Piironen, P.: 1994, *A High Spectral Resolution Lidar Based on an Iodine Absorption Filter*. Ph.D. thesis, University of Joensuu, Finland.

Roy, G., L. Bissonnette, C. Bastille, and G. Vallee: 1999, Retrieval of droplet-size density distribution from multiple-field-of-view cross-polarized lidar signals: theory and experimental validation. *Appl. Opt.*, **38**, 5202–5210.

Roy, G., L. R. Bissonnette, C. Bastille, and G. Vallee: 1997, Estimation of cloud droplet size density distribution from multiple-field-of-view lidar returns. *Opt. Eng.*, **36**, 3404–3415.

Shipley, S. T., D. H. Tracy, E. W. Eloranta, J. T. Trauger, J. T. Sroga, F. L. Roesler, and J. A. Weinman: 1983, High spectral resolution lidar to measure optical scattering properties of atmospheric aerosols. 1: Theory and instrumentation. *Appl. Opt.*, **22**, 3716–3724.

Stephens, G. L., S.-C. Tsay, P. W. S. Jr., and P. J. Flatau: 1990, The relevance of the microphysical and radiative properties of cirrus clouds to climate and climate feedback. *J. Atmos. Sci.*, **47**, 1742–1753.

Stephens, G. L. and P. J. Webster: 1981, Clouds and climate: Sensitivity to simple systems. *J. Atmos. Sci.*, **38**, 235–247.

van de Hulst, H. C.: 1957, *Light Scattering by Small Particles*. John Wiley and Sons, New York, N.Y., reprinted 1981 by Dover Publications, New York, N.Y.

Wielicki, B. A., R. D. Cess, M. D. King, D. A. Randall, and E. F. Harrison: 1995, Mission to planet earth: Role of clouds and radiation in climate. *Bull. Amer. Meteor. Soc.*, **76**, 2125–2153.

Wylie, D. P., W. P. Menzel, H. M. Woolf, and K. L. Strabala: 1994, Four years of global cloud statistics using HIRS. *J. Climate*, **7**, 1972–1986.

Wyser, K.: 1998, The effective radius in ice clouds. *J. Climate*, **11**, 1793–1802.

**DISCARD THIS PAGE**

# Appendix A: Instrumentation

The following section contains detailed information about the HSRL instrumentation and the computers used to make the Monte Carlo and multiple scatter calculations.

Table A.1 HSRL Transmitter Specifications

| **P**arameter | **V**alue |
|---|---|
| Wavelength | 532.112 nm |
| Frequency Stability | $<$ 50 MHz / hour |
| Spectral Width (FWHM) | $<$ 0.5 pm (SLM) |
| Pulse Duration | 180 ns |
| Pulse Repetition Rate | 4 kHz |
| Average Power | 0.25 W |
| Beam Profile | Gaussian $(TM_{\circ\circ})$ |
| Beam Diameter after Expansion | 4 cm |
| Beam Divergence after Expansion | $<$ 0.13 mrad |
| Polarization Type | Linear($>$1:1000) |
| Polarization Direction | Alternate $\parallel$ or $\perp$ |
| Polarization Switching Rate | 2 kHz |

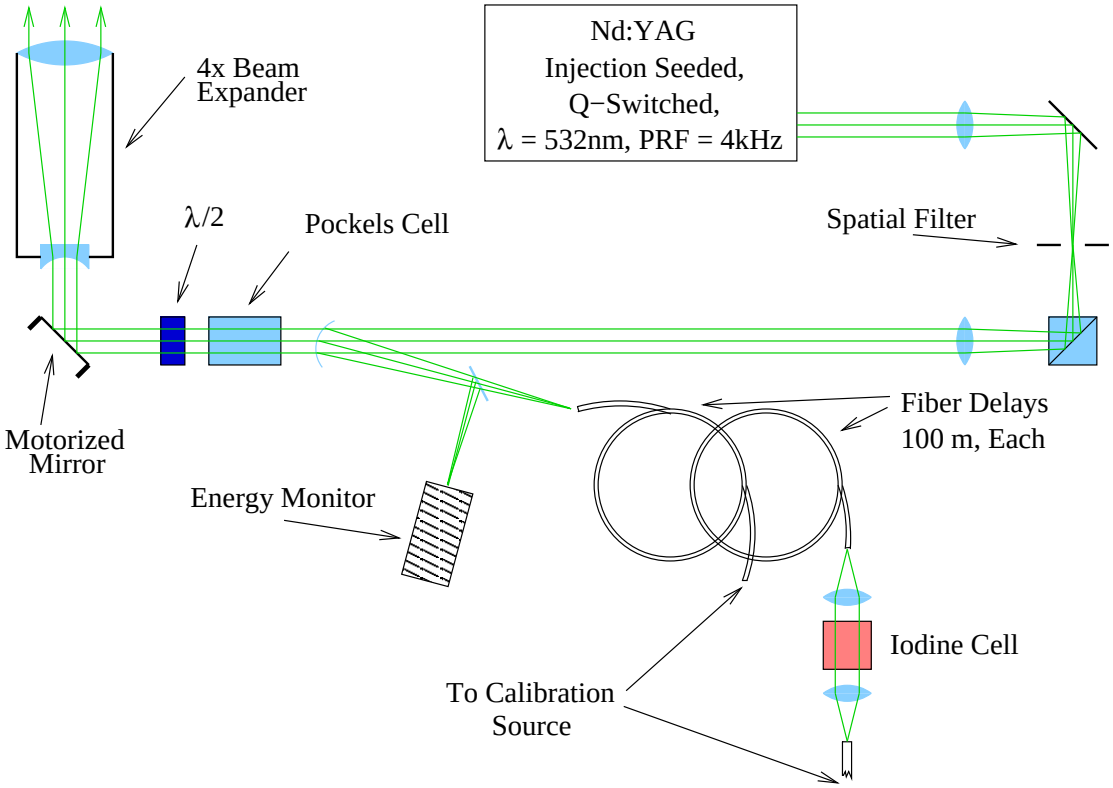


Figure A.1 A diagram of the HSRL transmitter. *Laser*: Produces a pulse of 1024 nm light that is frequency doubled using a KTP crystal to 532 nm. *Spatial filter*: This is a 200 $\mu$m aperture that prevents photons from being transmitted that are traveling outside of the main beam. *Fiber delays*: These are used to delay the transmitted pulse so the light from the calibration source can be observed after the data system has been triggered. *Iodine Cell (4 cm)*: Is used to wavelength-lock the laser to the peak of the iodine absorption spectrum. *Energy monitor*: The pulse energy is measured for each laser pulse so that the lidar profiles can be normalized by the pulse energy. *Pockels cell*: When a high voltage ( 1000 V) is applied to the Pockels Cell, the cell becomes a half-wave plate and will rotate the pulse polarization by $180°$. *Have-wave plate* ($\lambda/2$): Is used to rotate the pulse polarization by $180°$. It also facilitates the alignment of the transmitted polarization angle with respect to the receiver optics. *Motorized Mirror*: Is used to precisely align the transmitter pointing direction to the receiver narrow field-of-view. *Beam expander (4x)*: Is used to expand the beam diameter, this reduces both the pulse energy per unit area (for eye safety reasons), and the beam divergence.

Table A.2 HSRL Receiver Specifications

| **P**arameter | **V**alue |
|---|---|
| Telescope Type | Dall-Kirkham |
| Telescope Diameter | 0.5 m |
| Telescope Effective Focal Length | 5.08 m |
| Interference Filter Bandwidth | 0.3 nm |
| Fabry-Perot Etalon Bandwidth (daytime) | 8 pm |
| Cross-Polarization Rejection | $10^{-3}$ |
| **N**ARROW FOV | |
| Fixed FOV | 0.11 mrad |
| *Iodine Transmission Channel:* | |
| Signal Detected | Molecular |
| Detector Type | APD (Geiger Mode) |
| $I_2$ Notch Filter Bandwidth (FWHM) | 1.8 pm |
| *Direct Channel:* | |
| Signal Detected | Aerosol + Molecular |
| Detector Type | PMT |
| **A**NNULAR FOV | |
| Adjustable Annular FOV (Computer Controlled) | 0.11 - 2.2 mrad |
| *Iodine Transmission Channel:* | |
| Signal Detected | Molecular |
| Detector Type | PMT |
| $I_2$ Notch Filter Bandwidth (FWHM) | 1.8 pm |
| *Direct Channel:* | |
| Signal Detected | Aerosol + Molecular |
| Detector Type | PMT |

Table A.3 HSRL Data Acquisition System Specifications

| **P**arameter | **V**alue |
|---|---|
| Detection Mode | Photon Counting |
| Maximum Range | 35 km |
| Range Resolution | 15 m |
| Number of Counters | 4 |
| Counters Max. Counting Rate | 1 GHz |
| Number of Range Bins Available | 8192 / Channel |
| Number of Bins Used (Laser PRR Limited) | 2333 / Channel |
| Min. Bin Width (Variable) | 100 ns |
| Number of Data Buffers | 8 (2 polarizations / Channel) |
| Number of Returns Cumulated | 4000 |
| Data Acquisition Computer | Embedded Intel i960CA |
| Real-Time Control & Display Computer | DEC Alpha 333 Mhz |
| Connection interface between Computers | Ethernet |

Table A.4 Monte Carlo, Computer Specifications

| **P**arameter | **V**alue |
|---|---|
| Manufacturer | Dell |
| Model | PowerEdge 4400 |
| Number of Processors | 2 |
| Processor Type | Pentium Xeon |
| Processor Speed | 1.0 Ghz |
| $2^{nd}$ level cache size | 512 Kb |
| Memory Size | 4 GB |
| Operating System | Linux, kernel version 2.4 |

Table A.5 Gaussian approximate multiple scattering model, computer specifications

| **P**arameter | **V**alue |
|---:|---|
| Manufacturer | Generic |
| Number of Processors | 2 |
| Processor Type | Pentium III |
| Processor Speed | 900 Mhz |
| $2^{nd}$ level cache size | 512 Kb |
| Memory Size | 512 MB |
| Operating System | Linux, kernel version 2.2 |

# Appendix B: FOV-Aperture Mapping

Figure B.1 demonstrates the principle of separating photons from different fields of view on the focal plane of the receiving telescope.

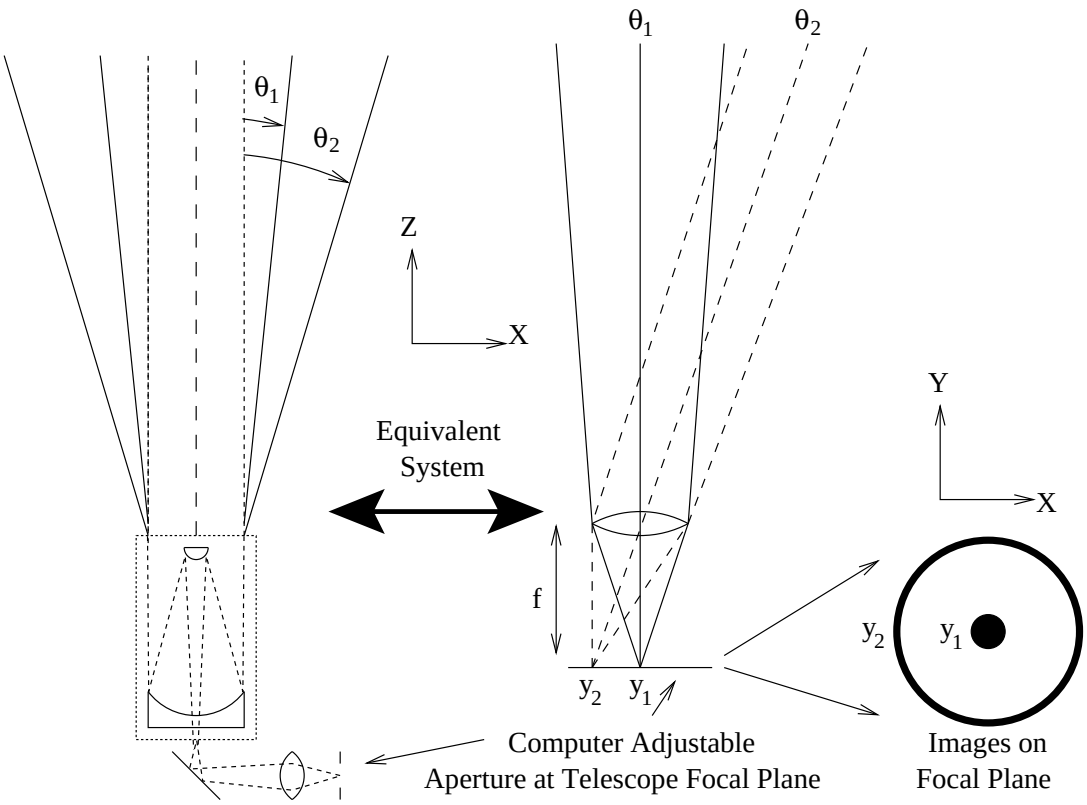


Figure B.1 Conceptual diagram of the HSRL wide field receiver, illustrating how different fields of view are mapped onto the focal plane. Light entering the receiver with an angle $\theta_2$ would produce an image on the focal plane designated by the ring $y_2$. The equation describing the position on the focal plane is $y \sim \theta \cdot f$ , where f is the effective focal length of the receiving telescope. So, light entering the receiver with an angle $\leq \theta_2$ would fill in the entire circle with a radius $\leq y_2$. By changing the size of the aperture on the focal plane the field of view of the receiver is changed.